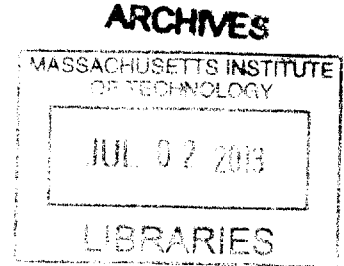# Decoupling bulk- and surface-limited lifetimes in thin kerfless silicon wafers using spectrally resolved transient absorption pump-probe spectroscopy and computer simulations

by

Sin Cheng Siah

B. Eng., Engineering Science
National University of Singapore, 2010

Submitted to the Department of Mechanical Engineering
in partial fulfillment of the requirements for the degree of
Master of Science in Mechanical Engineering

at the

MASSACHUSETTS INSTITUTE OF TECHNOLOGY

June 2013

Author...
Department of Mechanical Engineering
May 10, 2013

Certified by..
Tonio Buonassisi
Associate Professor of Mechanical Engineering
Thesis Supervisor

Accepted by.....................................
David E. Hardt
Professor of Mechanical Engineering
Chairman, Department Committee on Graduate Theses

Decoupling bulk- and surface-limited lifetimes in thin kerfless silicon wafers using spectrally resolved transient absorption pump-probe spectroscopy and computer simulations

by

Sin Cheng Siah

Submitted to the Department of Mechanical Engineering
on May 10, 2013 in Partial Fulfillment of the
Requirements for the Degree of Master of Science in
Mechanical Engineering

ABSTRACT

One of the key technological objectives to further decrease the cost of silicon (Si) PV and enable manufacturing of crystalline silicon is to improve the quality of thin, kerfless Si wafers to monocrystalline equivalent. To aid wafer manufacturers to develop high-quality thin Si wafer substrates, performance-limiting defects in the bulk of thin kerfless Si wafers must be identified, and a means to accurately measure the bulk lifetime is necessary. With decreasing wafer thickness, however, the impact of surface recombination increases and dominates the effective lifetime measured by conventional methods. Therefore, the ability to decouple bulk-limited lifetime from surface-limited lifetime is desirable, ideally without the need for surface passivation.

Herein, spectrally resolved transient absorption pump-probe spectroscopy and extensive Technology Computer Aided Design simulations are used to decouple

the bulk- and surface-limited lifetimes of thin kerfless silicon wafers in a single measurement. A range of sample conditions are studied. It is observed that the technique can successfully provide reasonable upper and lower limits to the bulk and surface recombination parameters for thin kerfless silicon wafers.

Thesis Supervisor: Tonio Buonassisi
Title: Associate Professor of Mechanical Engineering

ACKNOWLEDGEMENTS

CONTENTS

9

FIGURES

11

13

CHAPTER

1

INTRODUCTION

1.1 Sustainable Energy Source

During the industrial revolution in the 18th century, there was a heavy demand for mechanical machines to drive manufacturing processes. Demand for energy in the form of fossil fuels to power these machines increased dramatically and since then, mankind never looked back. Global energy consumption is now estimated to be 1.7×10^{14} kW·h and is expected to grow by 53% over the next 20 years [1]. While standard of living has improved as a result of this revolution, continued unsustainable use of resources to meet our insatiable thirst for energy has resulted in undesirable impacts on Earth's environment. This has led to a plethora of problems that include air and water pollution, depletion of natural resources and global change. According to a report published by the International Panel on Climate Change (IPCC), high-accuracy measurements have provided evidence for the direct correlation between warming of the Earth's atmosphere to human activities. Consequently, climate champions such as former U.S. Vice president Al

Gore and the IPCC have strongly advocated for the mitigation of these negative impacts on the Earth's climate by moving towards a future that is built upon energy sustainability.
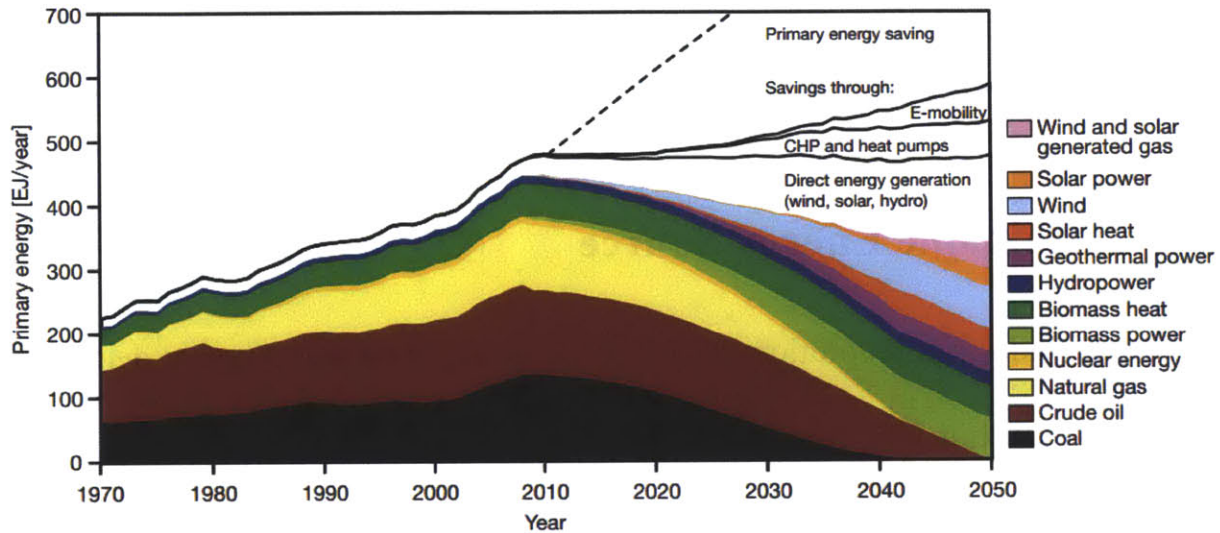
Figure 1.1: Distribution of global primary energy demand by 2050 as predicted by the German Advisory Council on Global Change, from Reference [2]. The scenario is predicted based on extrapolation of current expansion rates of various renewable energies.

A viable option to reduce mankind's reliance on conventional energy sources is to adopt renewable energies as alternatives. As illustrated in Figure 1.1, the German Advisory Council on Global Change envisions several renewable energy options that are expected to be more important by 2050. It can be seen that conventional fossil fuels are not expected to be totally replaced but their overall contribution is expected to decrease significantly over the next 40 years. On the other hand, renewable energies are expected to increase their relative contribution to the

16

energy distribution. In particular, solar is an attractive alternative due to the vast amount of energy Earth receives from the sun every day. To put things into perspective, the Earth receives about 5.5×10^{17} kW·h of energy from the sun annually. This is about 3200 times the world total energy consumption in 2013. Solar energy can be harvested in the form of heat (solar thermal) or electricity (photovoltaics). In this thesis, the main focus will be on photovoltaics (PV). The goal of solar PV is to convert a fraction of this enormous resource from the sun into electricity for immediate use or short-term storage.

1.2 Potential of Crystalline Silicon Solar Cells

Photovoltaics involves the direct generation of electricity from sunlight via the PV effect. The photovoltaic effect was discovered by French physicist A. E. Becquerel in 1839 while experimenting with solid electrodes immersed in an electrolyte solution. He observed that a voltage was developed when light fell upon the electrode. It was not until 1954 when the first practical solar PV device based on crystalline silicon (c-Si) with an energy conversion efficiency of ~6% was introduced by Chapin *et al.* at AT&T Bell Laboratories [2].

2010 Cell Production by Technology (MW-dc)
Total: 23,889 MW

CIS/CIGS, 426, 2%
Thin film Si 1,349, 5%
CdTe, 1,438, 6%
Super Monocrystalline Si, 920, 4%
Standard Crystalline Si, 19,768, 83%
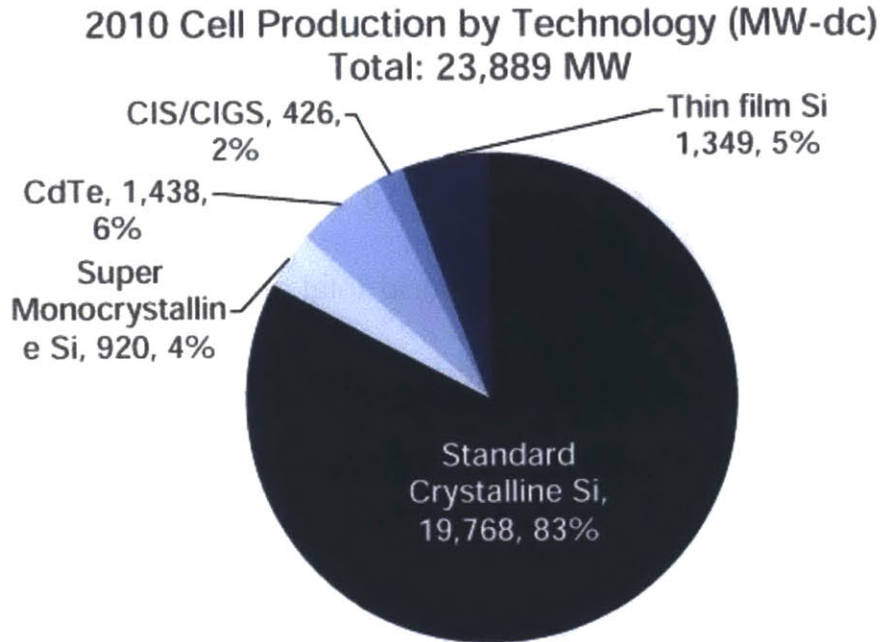
Figure 1.2: Solar cell production by technology in 2010, from Reference [3].

As shown in Figure 1.2, standard c-Si solar cells make up over 87% of the PV industry in 2010. The remainder of the PV market consists of solar cells based on thin film technologies such as amorphous silicon, cadmium telluride and copper indium gallium diselenide [3].

At present, numerous barriers still exist for c-Si PV modules to be cost competitive with current base load fossil-fuel electrical utility plants. The recent Department of Energy (DOE) SunShot Initiative sets a very aggressive goal for solar energy to reach a Levelized Cost of Energy (LCOE) of US$0.06/ kW·h by 2020 with no incentives or tax credits. This translates to PV module costs of US$0.50-0.75 per peak watt (W_p) [4]. However, current c-Si manufacturing costs are about a factor

of two to three times higher than the US$0.50/$W_p$ target. As a result, cost-reduction of PV electricity is required to attain grid competitiveness.

1.3 Cost-reduction Research Trends for c-Si PV

While part of the cost-reduction can be obtained through economy-of-scale, the c-Si PV community is also actively pursuing research domains that have large cost-reduction potential. Powell *et al.* [4] developed a comprehensive cost-analysis framework for identifying technology pathways that provide the greatest cost-reduction potential. From the feedstock to module level, the main research trends can be broadly classified into three categories, namely reducing Si usage, attaining higher conversion efficiencies and reducing manufacturing-related costs. The various technological requirements to support these research trends are summarized in Figure 1.3.

19
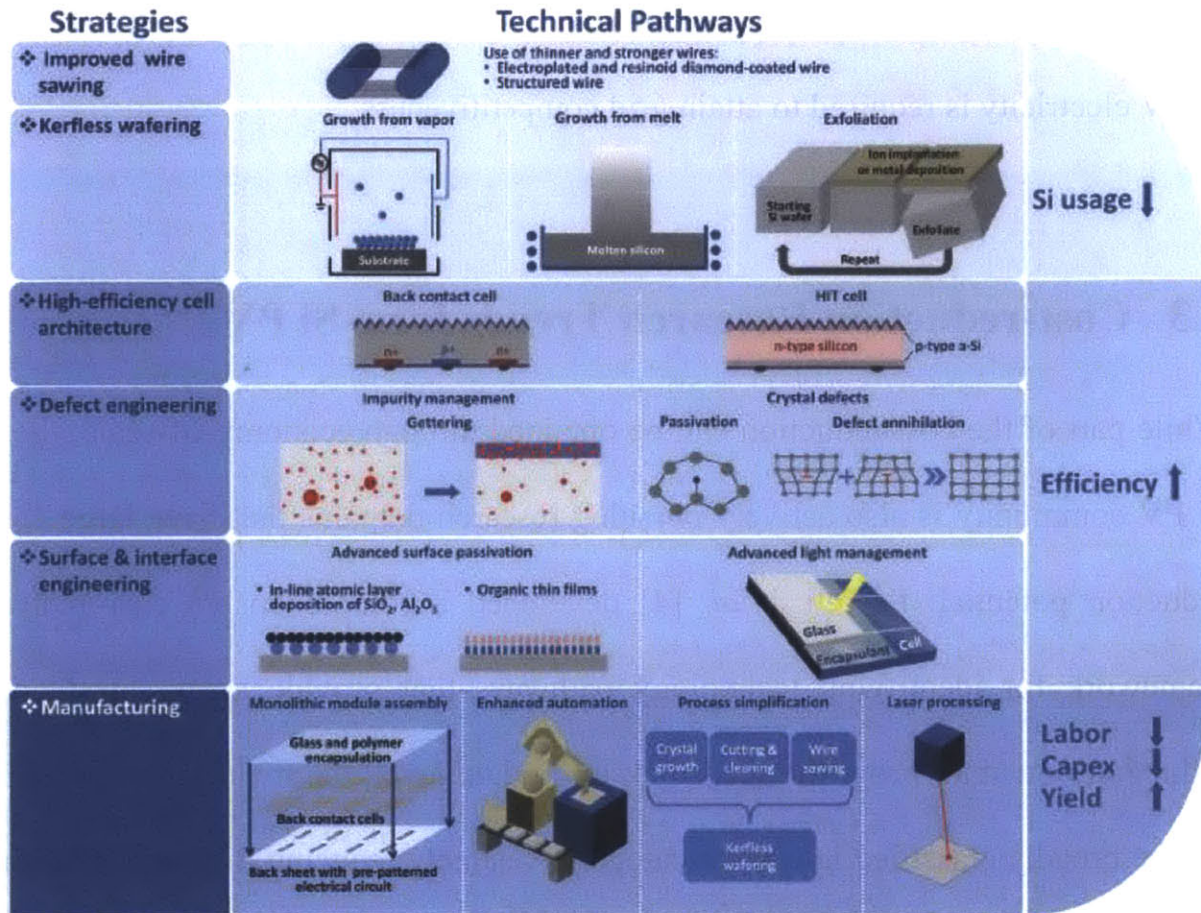
Figure 1.3: Technology pathways to achieve US$0.50/W$_p$ module cost target, from Reference [4].

1.4 Motivation of Research

One key innovation area highlighted by Powell *et al.* is a high-efficiency cell architecture for thin kerfless wafers [4]. To aid wafer manufacturers to develop high-quality thin Si wafer substrates, performance-limiting defects in the bulk of thin kerfless Si wafers must be identified, and a means to accurately measure the bulk lifetime is necessary. Most lifetime-measurement techniques produce only an

effective lifetime, which is a combination of the bulk- and surface-limited lifetime. A sample with a high bulk and low surface lifetime might not be distinguishable from a sample with a low bulk and high surface lifetime, although the bulk lifetime is the parameter that determines solar-cell device performance potential. Furthermore, with decreasing wafer thickness, the impact of surface recombination increases and dominates the effective lifetime measured by conventional methods [5]. Therefore, the ability to decouple bulk-limited lifetime from surface-limited lifetime is desirable, ideally without the need for any modifications to the bare c-Si wafers such as depositing a layer of dielectric for surface passivation. In this thesis, spectrally resolved transient absorption pump-probe spectroscopy and extensive Technology Computer Aided Design (TCAD) simulations are used to decouple the bulk- and surface-limited lifetimes of thin kerfless silicon wafers in a single measurement.

1.5 Thesis Outline

The work described in this thesis was carried at the Photovoltaic Research Laboratory at Massachusetts Institute of Technology. This work aims to measure the bulk- and surface-limited lifetimes of thin kerfless silicon wafers in a single,

non-destructive measurement so that the effectiveness of defect engineering techniques on deleterious defects can be investigated.

Chapter 2 is concerned with introducing the concepts of carrier generation and recombination in physical terms. In particular, the different generation and recombination mechanisms in semiconductors are introduced and their relative importance in c-Si is discussed. The way in which these various recombination mechanisms combine to produce a so-called effective lifetime through the Matthiessen's rule is also mentioned. In order to emphasize the importance of carrier lifetime, the effects of recombination on the critical parameters of thin kerfless c-Si solar cell performance are given. An overview of the various methods that are commonly used contactless photo-conductance decay measurements to measure the effective lifetime are presented and the technique that is most interested in this thesis, spectrally resolved transient pump-probe spectroscopy is introduced. Lastly, the various experimental techniques used to decouple bulk- and surface-limited lifetime will be introduced.

Chapter 3 is focused on introducing the basic physical concepts, including the optical generation model and governing transport equations that are required to describe the dynamics of photo-generated carriers in c-Si wafer. In addition, the boundary conditions that describe the recombination of carriers at the surface and the doping dependent mobility model are introduced. In this work, TCAD

simulation is performed using the Sentaurus package [6] by Synopsys and the various components of the Sentaurus package will be summarized briefly.

Chapter 4 describes the process of decoupling bulk- and surface-limited lifetime. The numerical fitting procedure is first introduced and extensive error analysis is performed to characterize and quantify the source of both random and systematic error in the technique. The error analysis provides a confidence limit for the fitted parameters.

In chapter 5, the main findings and results of this work is summarized. A total of four samples with a range of conditions composing of both thick and thin wafers and different surface layers are characterized. Finally, chapter 6 concludes the main research findings.

2

CARRIER GENERATION AND RECOMBINATION

2.1 Generation, Recombination and Effective Lifetime

The various band-to-band generation and recombination process are shown schematically in Figure 2.1. In the process of generation, electrons are excited from the valence band to the conduction band. The energy of transition can either be supplied by an incoming photon (optical absorption) or multiple phonons (thermal generation). Recombination refers to the inverse process whereby electron-hole pairs are annihilated due to the transition of excited electrons from the conduction band of a semiconductor into unoccupied states in the valence band. In this process, the excess energy is released as photons (radiative recombination) or phonons (thermal recombination) or transferred to other carriers (Auger recombination). Thermal generation and recombination are very rare in common semiconductors due to the large difference between ambient thermal energy (0.026 eV at room temperature) and the bandgap energy (1.12 eV).
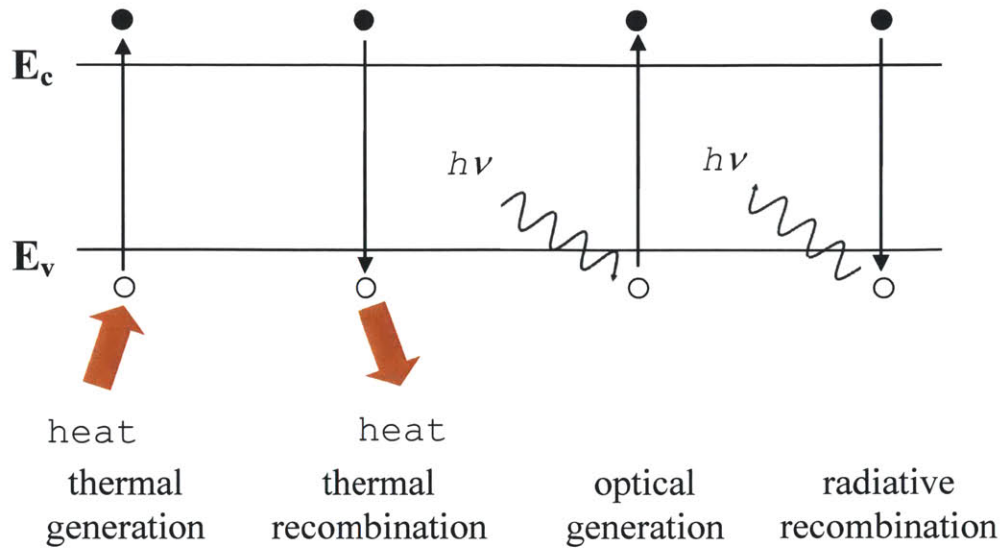
Figure 2.1: Schematic diagram of band-to-band generation and recombination mechanisms.

A semiconductor in thermal equilibrium at non-zero temperature is a highly dynamic system. Electrons and holes are continuously generated and recombined through the breaking and re-forming of covalent bonds. The principle of detailed balance states that the generation and recombination rates of each process must balance out precisely. This implies that:

$$G_{0i} = R_{0i} \tag{2.1}$$

where G and R are the generation and recombination rates [cm^{-3}s^{-1}] respectively in thermal equilibrium; the subscript "0" denotes thermal equilibrium and "i" denotes the various generation-recombination processes. This dynamic process leads to the equilibrium electron (n_0) and hole (p_0) densities.

In the case of optical excitation, the total generation rate is increased $G > G_0$ which has to be counter-balanced by an increased recombination rate $R > R_0$ so that a new

equilibrium state can be reached. When the external optical generation source is switched off, the excited system will trend back towards its thermal equilibrium state by reducing the excess photo-generated electron (Δn) and hole (Δp) densities [cm^{-3}]. However, this process does not occur instantaneously as the excess carrier densities decay according to the net recombination rate $U = R - R_0$, which is characteristic of all the recombination processes in the system. By assuming that $\Delta n \approx \Delta p$, the transient decay of excess carriers can be described using a simple first order differential equation:

$$\frac{\partial \Delta n}{\partial t} = -U(\Delta n(t), n_0, p_0) \tag{2.2}$$

Equation 2.2 can be simplified into a linear first-order partial differential equation (PDE) by expressing U only as a linear function of Δn:

$$U(\Delta n(t), n_0, p_0) = \frac{\Delta n(t)}{\tau_{eff}} \tag{2.3}$$

where τ_{eff} is a constant and typically known as the effective carrier lifetime. By solving the linear first-order PDE, the time-dependent decay of Δn follows an exponential law with a decay time constant of τ_{eff}. In first approximation, τ_{eff} can often be expressed as a combination of the various recombination lifetimes (radiative, Auger, trap-assisted Shockley-Read-Hall (SRH) and surface) using Matthiessen's rule:

$$\frac{1}{\tau_{eff}} = \frac{1}{\tau_{radiative}} + \frac{1}{\tau_{Auger}} + \frac{1}{\tau_{SRH}} + \frac{1}{\tau_{surface}} \qquad (2.4)$$

where the bulk lifetime is the combination of the radiative, Auger and SRH lifetimes:

$$\frac{1}{\tau_{b}} = \frac{1}{\tau_{radiative}} + \frac{1}{\tau_{Auger}} + \frac{1}{\tau_{SRH}} \qquad (2.5)$$

and the surface lifetime can be expressed as:

$$\frac{1}{\tau_{surface}} = 2\frac{S_{eff}}{d} \qquad (2.6)$$

where S_{eff} is the effective surface recombination velocity [cm/s] and d [cm] is the thickness of the semiconductor, assuming both surfaces have similar S_{eff}. The reciprocal sum of lifetimes in Equation 2.4 implies that the mechanism with the smallest lifetime dominates the recombination dynamics of the semiconductor. Note that Equation 2.6 is an approximation, valid in the limit of low S_{eff} and thin wafers (*i.e.*, when carrier diffusion to a surface is not the rate-limiting step for recombination).

However, Equations 2.2–2.4 are generally inadequate to describe the dynamics of photo-generated carrier densities and have to be used with proper knowledge about the assumptions involved. Equation 2.2 neglects carrier transport by assuming spatially homogenous generation of excess carriers within the bulk and negligible electric field. Furthermore, by expressing U as a linear function of Δn, low-level

28

injection condition whereby $n_0 \ll \Delta n \ll p_0$ is assumed (for a p-type semiconductor). Consequently, to describe the dynamics of excess carrier densities under all injection conditions and spatially non-homogenous generation profiles, more detailed models that take into account carrier transport through drift and diffusion, injection-dependent lifetime models and proper boundary conditions are required. Such concerns will be addressed in Chapter 3 using TCAD simulation.

2.2 Mitigating Lifetime-Limiting Mechanisms in Thin Kerfless c-Si Solar Cells

2.2.1 Effects of Surface Recombination

Surface recombination can have a significant impact on efficiency with decreasing wafer thickness [7]. As shown in Figure 2.2, experimental measurements found that the efficiency of 14 μm thin inter-digitated back-contact c-Si solar cells can vary over a wide range depending on the quality of surface passivation [8].

Consequently, outstanding surface passivation is required to achieve high-efficiency thin kerfless c-Si solar cells. By using a thin layer of amorphous silicon (a-Si) in a heterojunction with intrinsic thin layer (HIT) cell structure [9], Sanyo has successfully demonstrated that the open-circuit voltage (V_{oc}) of HIT cells increases with decreasing wafer thickness [10]. A high V_{oc} of 747 mV with 58 μm

thin c-Si wafers has been demonstrated and one of the main reasons for this achievement is the excellent surface passivation by a-Si film [10]. Other surface strategies include amorphous silicon nitride (a-Si$_x$N$_y$:H) [11] and Al$_2$O$_3$ [12] which have all demonstrated excellent surface passivation qualities.

Key	Efficiency	Coating	Annealing type	Anneal time and temperature
· · · · ·	1.24%	N/A	N/A	N/A
· · · · · · ·	2.95%	ALD alumina	Hot plate	30 min at 430°C
― ―	4.14%	ALD alumina	Oven forming gas	30 min at 430°C
· · · · · · · ·	5.94%	Nitride: low ammonia, low RF, high temp	N/A	N/A
― ―	7.40%	Nitride: high ammonia, high RF, high temp	N/A	N/A
· · · · · ·	10.30%	Optimized nitride	Oven forming gas	1 hr at 450°C
― ―	12.20%	Optimized nitride	Oven forming gas	2 hr at 450°C
——	14.86%	Optimized nitride	Oven forming gas	3 hr at 450°C

Figure 2.2: *J-V* curves of 14 μm thin interdigitated back-contact c-Si solar cells with various surface passivation strategies, from Reference [8].

2.2.2 Effects of Bulk Recombination

To reduce costs of c-Si PV, low-cost feedstock materials are being developed and utilized. The use of these low-cost alternative materials will most probably lead to c-Si with a much higher concentrations of deleterious transition metal impurities, which can lead to significant bulk recombination losses. In addition to bulk metal

30

impurities, bulk defects in the form of dislocations have been shown experimentally to be detrimental towards cell performance. In the context of kerfless c-Si, dislocations can be introduced during the epitaxial growth or exfoliation process [13]. Experimental measurements on 2 μm thin c-Si solar cells grown epitaxially on c-Si wafers have shown that an increase in dislocation density causes the V_{oc} to degrade [13], [14].

Extensive research has been carried out to mitigate the impact of these bulk defects in commercially available c-Si. For example, nanodefect metal impurity engineering and phosphorous gettering are different strategies that can be used to mitigate the impact of transition metal impurities in the bulk [15]. High-temperature annealing can also be performed to reduce the dislocation density in multicrystalline silicon wafers [16]. However, the effectiveness of these techniques on kerfless silicon is still a relatively new area of research. To achieve high-efficiency solar cells using thin kerfless c-Si wafers, it is therefore crucial to identify the deleterious bulk defects and develop feasible strategies to mitigate their impacts on cell performance.

2.3 Lifetime Characterization Techniques

2.3.1 Measuring Bulk- and Surface-Limited Lifetimes

In the previous section, the significance of surface and bulk recombination toward cell efficiency is discussed. The figure-of-merits of interest are the bulk lifetime, τ_b, and the effective surface recombination velocity S_{eff}. Unfortunately, both quantities are combined together through Equation 2.4, and τ_{eff} is the quantity that is being measured. Hence, the common practice for measuring S_{eff} involves using c-Si wafers grown by the float zone process. As these wafers have a high τ_b, the measured τ_{eff} is dominated by recombination losses at the surfaces at low injection condition and by assuming infinite τ_b, an upper limit for S_{eff} can be determined. In a similar way, τ_b of a c-Si wafer can be measured if excellent surface passivation is applied on both surface of the c-Si wafer such that the dominant mechanism is bulk recombination.

2.3.2 Inductively-coupled Photoconductance Decay Technique

The most common technique used to determine of photo-generated carriers is the inductively-coupled photoconductance technique commercialized by Sinton Consulting [17], as shown schematically in Figure 2.3. The change in conductance of the sample due to photo-generation by an external light flash source induces a

change in inductance in the coil due to the proximity of the sample to the coil. The

decay in photoconductance is measured by the radio-frequency electronics.
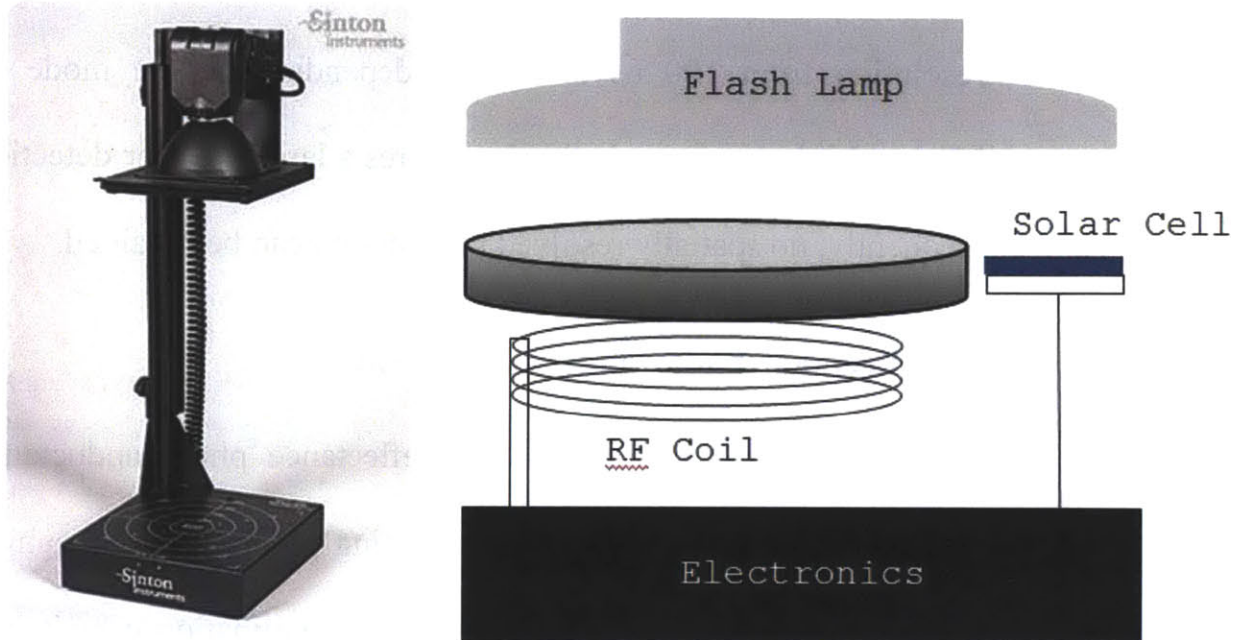
Figure 2.3: The photo on the left is the Sinton WCT 120 silicon wafer lifetime tester and the figure on the right is a schematic illustration of the tool.

This technique can be operated in two different modes by changing the flash

duration of the illuminating lamp. In the transient photoconductance decay (PCD)

mode, a short flash (~15 µs) is used and a long flash (~2 ms) is used in the quasi-

steady-state photoconductance (QSSPC) mode. Typically, the PCD mode is

suitable for measuring samples with high τ_{eff} whereas the QSSPC mode is suitable

for samples with low τ_{eff}, comparatively to the flash duration. Homogenous

generation within the sample is ensured by using an infrared filter and the effective

lifetime can be determined as function of injection level by measuring the photoconductance decay and light intensity at the same time.

Due to the contactless nature, this technique is non-destructive. It also has a very wide temporal resolution from 100 ns to 10 ms, depending on the mode of operation. A major drawback, however, is that it requires a large area for detection (~6 cm^2) and consequently, no spatially resolved information can be obtained.

2.3.3 Microwave Reflectance Photoconductance Decay

Another method of measuring τ_{eff} is microwave reflectance photoconductance decay (μ-PCD). The microwave-absorbing and -reflecting properties of a sample change upon external illumination. Immediately after the illumination is switched off, the transient decay of excess carriers in the sample causes the reflected microwaves to vary with a time dependence that is related to the conductivity of the sample. As illustrated in Figure 2.4, the microwave is generated and directed onto the sample via a waveguide. At the same time, excess carriers are photo-generated using a pulsed laser and the change in photoconductivity is measured based on the change in the amount of microwave being reflected off the sample.
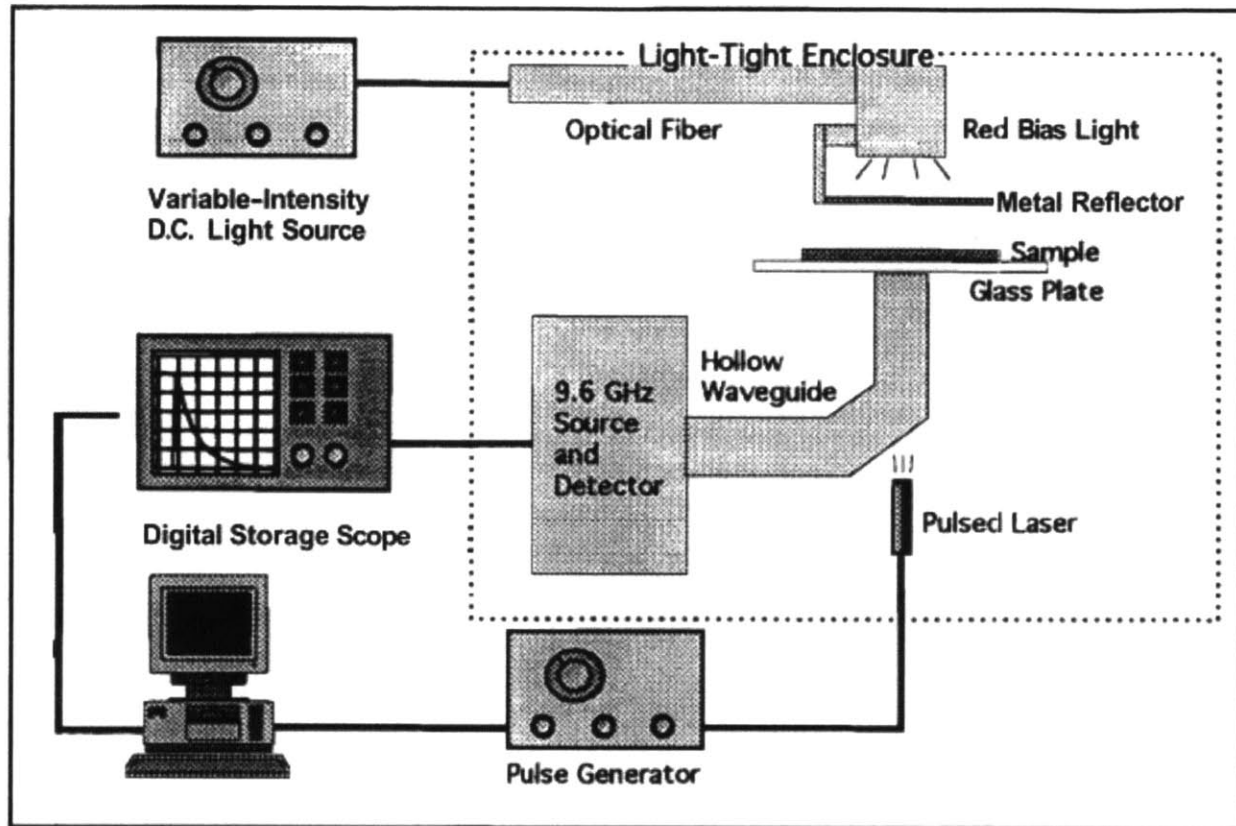
Figure 2.4:Schematic diagram of the μ-PCD tool, from Reference [18].

Due to the contactless nature, this technique is non-destructive. In addition, this technique has good spatial resolution due to the small laser spot size (down to 0.5 mm). The injection dependence of the measurement can be modified by applying a known bias light to vary the injection condition. The main drawback of this technique is its temporal resolution, which is limited by the pulse duration of the laser. For a WT-2000 Semilab tool, the temporal resolution is limited to >1 μs due to the pulse width of the excitation laser. While this resolution is sufficient for a well-passivated c-Si wafer, the τ_{eff} of an unpassivated, ungettered wafer can be

35

lower than 1 μs [19]. Another drawback of this technique is the surface sensitivity: The reflected microwave beam does not penetrate through the sample bulk, thus it only carries information about the surface concentration of electrons (which tends to be more heavily influenced by surface recombination).

2.3.4 Transient Free Carrier Absorption

Apart from using changes in inductance or microwave reflectance, changes in free carrier absorption (FCA) can also be used to detect the decay of excess carrier density. In FCA, photon energy (typically in the infrared) is absorbed by free carriers in either the conduction or valence band [20]. As shown in Figure 2.5, the absorption coefficient of silicon in the infrared increases with free carrier density and wavelength of incident radiation. Such property can be used to measure the transient decay of free carrier density through infrared transmission.
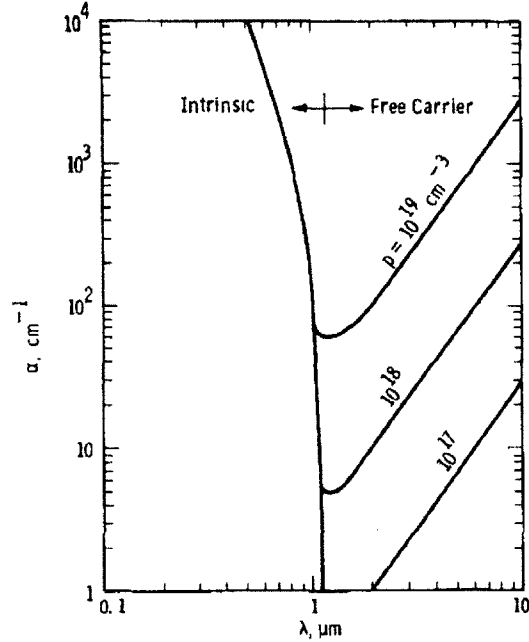
Figure 2.5: Intrinsic and free carrier absorption coefficients for silicon as a function of incident photon wavelength, from Reference [20].

Figure 2.6 illustrates schematically the typical experimental setup in which a pump-probe configuration is used. A pulsed laser is used as a pump to generate free carriers in the sample and a continuous wave infrared laser (HeNe 3.39 um) is used as a probe laser. Upon interaction of the pump beam with the sample, photo-generated free carriers will attenuate the intensity of the infrared probe beam and consequently, the transient decay of the free carrier density can be measured through the time dependence of infrared transmission.
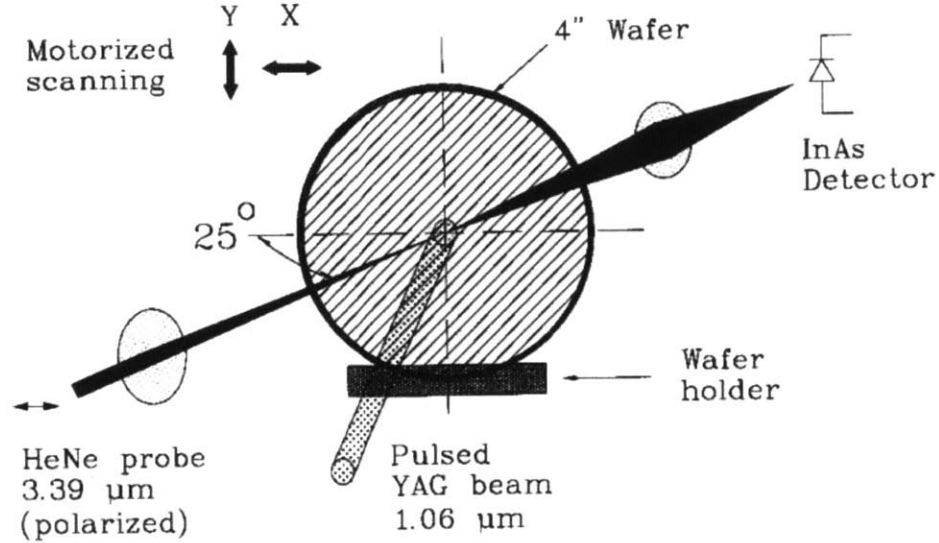
Figure 2.6: Schematic of the pump-probe setup, from Reference [21].

This technique offers a non-destructive approach to characterize τ_{eff}. The spatial resolution is limited by the spot size of the probing laser beam and can be focused down to <1 mm using optical lenses. Coupled with an X-Y motor stage, mapping capabilities can be achieved. The temporal resolution of this technique is mainly limited by the full width at half maximum (FWHM) of the incident pump laser pulse, the rise time of the photo-detector, and the response time of the read-out electronics. In the experimental apparatus reported herein, the FWHM of the pump laser pulse and the rise time of the detector can be as low as 5 ns.

2.4 Existing Methods to Decouple Bulk and Surface-Limited Lifetimes

As mentioned in previous section, the figure-of-merits of interest in lifetime measurements are the bulk lifetime, τ_b, and the effective surface recombination velocity S_{eff}. Unfortunately, both quantities are combined together and it is of interest to separate their contributions from the measured τ_{eff}. To this end, a number of methods have been proposed to decouple the bulk- and surface- limited lifetimes. However, most of them are destructive or require complicated surface modifications. Some of the more notable methods are examined in this section.

2.4.1 Two-wafer Method

One simple method to decouple τ_{eff} and τ_b is to make two wafers, I and II, where the thickness is such that $d_I = 2d_{II}$, while keeping the bulk and surface properties identical. By combining equations 2.4–2.6, the measured effective lifetime can be expressed as:

$$\frac{1}{\tau_{eff}} = \frac{1}{\tau_b} + 2\frac{S_{eff}}{d} \qquad (2.7)$$

With 2 sets of equations from wafer I and II, S_{eff} and τ_b can be solved for simultaneously [22]. Normally, the thinner wafer can be obtained be polishing down a thick wafer which is a destructive process. At the same time, the polishing

39

process can modify both the surface and bulk properties, thus introducing potential error into this technique.

2.4.2 Immersing Samples in Hydrofluoric Acid or Iodine/Methanol Solution

It was reported that S_{eff} on a c-Si surface can be as low as 1 cm/s when immersed in a bath of hydrofluoric acid [23]. The origin of this unusually low S_{eff} can be attributed to the passivation of dangling bonds on the surface through the formation of Si-H covalent bonds. With a very low S_{eff}, τ_{eff} is typically dominated by bulk recombination and $\tau_b \approx \tau_{eff}$. By performing a normal measurement prior to HF immersion, both S_{eff} and τ_b can be determined. Alternatively, halogens such as iodine or bromine in a methanol solvent have also been shown to exhibit excellent surface passivation with $S_{eff} < 1$ cm/s and can be used for the same purpose [24].

This technique is widely used to determine the "true" τ_b of c-Si wafers. However, the main disadvantage is that it is destructive in nature, as it modifies the surface chemistry, sometimes irreparably. In addition, liquid passivation techniques are known to be temporally unstable.

2.4.3 Dual Excitation Source Approach

Shorter-wavelength light is more strongly absorbed closer to the surface and hence more sensitive to surface recombination. Using this property, surface and bulk

40

recombination can be distinguished by measuring the transient decay of excess carrier density using excitation light with different wavelengths, λ. As shown in Figure 2.7(a), excitation light of different λ result in a separation δ between the decay profiles of photo-generated carrier density and δ is a function of S_{eff}. In Figure 2.7(b), first order model is being used to generate a look-up table for δ as a function of λ, d, S_{eff} and τ_b. By measuring δ, S_{eff} and τ_b can be inferred from the look-up table.

The main advantage of this technique is its non-destructive nature. However, the main drawback is that it only uses the asymptotic mono-exponential part of the decay. Hence, its sensitivity is limited to a certain region in the S_{eff} and τ_b space. As shown in Figure 2.7(b), δ saturates to a certain value depending on S. Consequently, the extracted pair of S_{eff} and τ_b is not a unique solution. To extend the sensitivity of this technique, it is important to take into account the multi-exponential phase of the decay signal at early time scales.
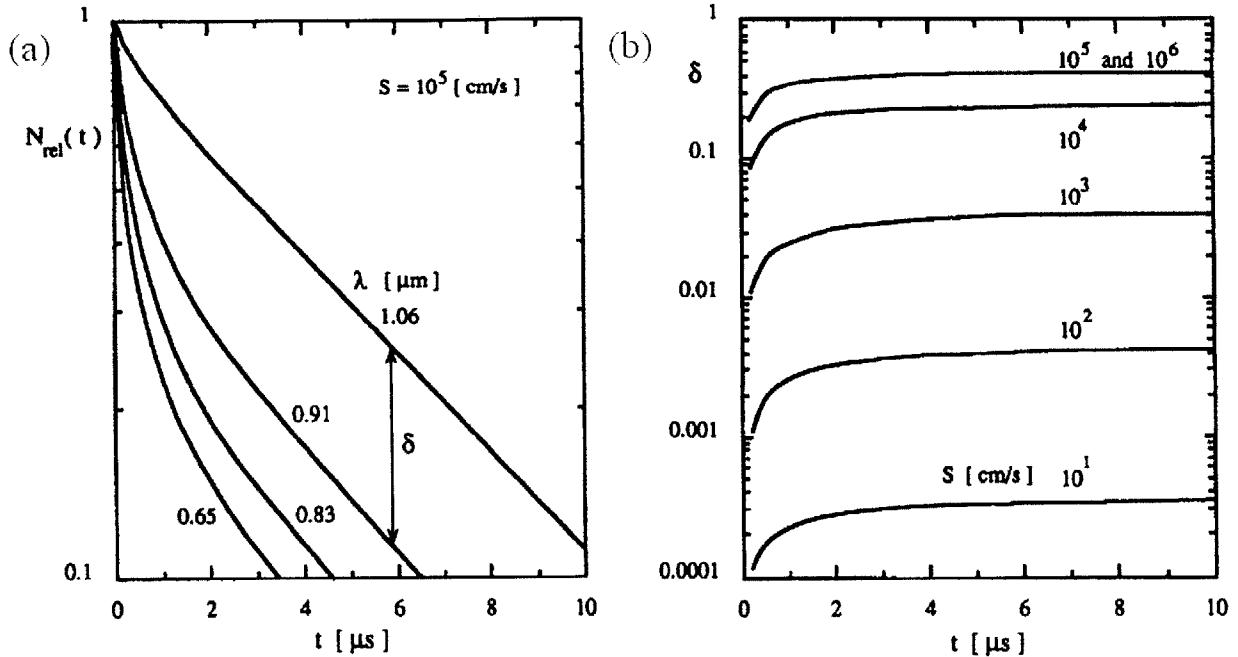
Figure 2.7: Decay profiles of the normalized excess carrier density for different values of λ and $d=$ 525 um. The separation between any 2 decay profiles is denoted by δ and, (b) δ as a function of S_{eff} and τ_b. Figures are from Reference [25].

2.5 Proposed Method to Decouple Bulk and Surface-Limited Lifetimes

In this work, a new approach to decouple the bulk and surface recombination parameters is proposed. Figure 2.8 represents the flow diagram that describes this new technique. Spectrally resolved transient pump-probe spectroscopy that is based on the principle of FCA is used to measure the decay transients of excess carrier density due to its good spatial and temporal resolution. Figure 2.9 shows the

schematic illustration of the lifetime measurement setup. A tunable-wavelength laser with a 6 ns FWHM is used as pump source; a monochromatic probe beam (1550-nm wavelength) is derived from a tungsten bulb and monochromator. In addition, a 6-GHz oscilloscope, a high-speed InGaAs photodetector (5-ns rise time), and a 40-dB amplifier are used for data collection. As compared to using the analytical solution which assumes an injection-independent recombination rate and constant carrier diffusion coefficients, TCAD software is used to solve the set of relevant semiconductor equations for both electrons and holes self-consistently, taking into account injection-dependent lifetime and concentration-dependent mobility models. Numerical fitting is used to minimize the mean squared error between the experimental and simulation results.

Measure sample thickness
and resistivity

Measure sample using
transient FCA

TCAD
Simulation

Numerical
Analysis

refine
parameters if
fit is poor

good fit

Extract Fit
Parameters
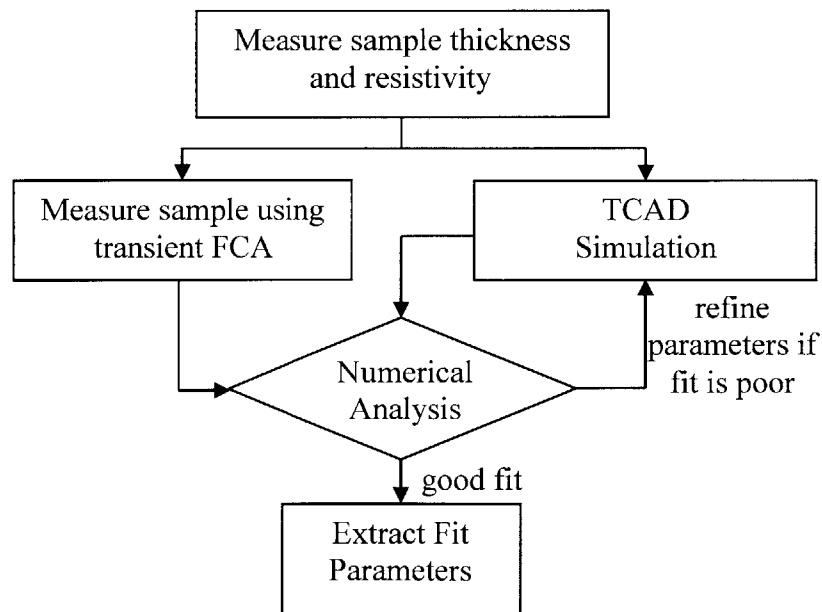
Figure 2.8: Flow diagram representing the process of decoupling the fit parameters.

43
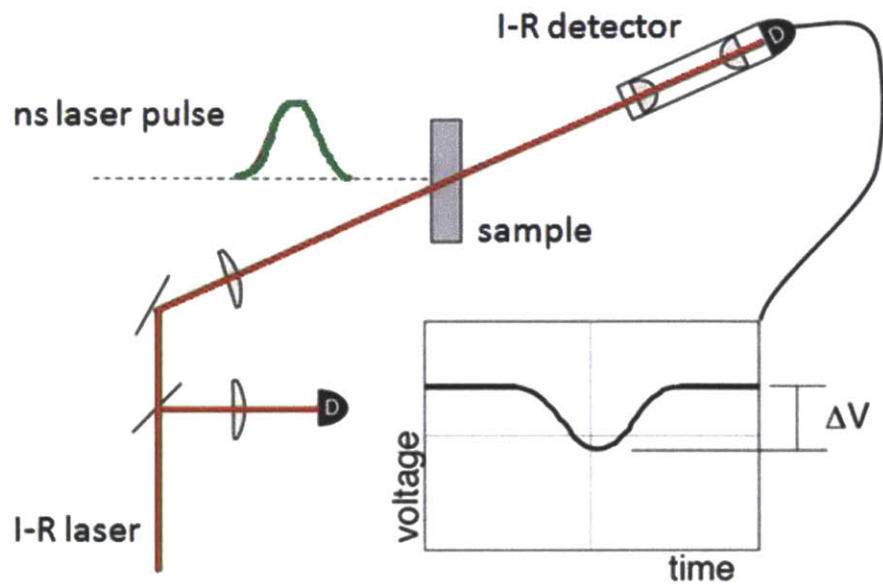
Figure 2.9: Schematic diagram of the spectrally resolved transient absorption pump-probe spectroscopy lifetime measurement technique, courtesy of Mark T. Winkler.

3

NUMERICAL MODELING: TCAD SOFTWARE

3.1 Introduction to TCAD Modeling

A major limitation of the decoupling techniques described in previous chapter is the use of relatively simple mathematical models. For example, carrier lifetimes are assumed to be independent of injection level, mobilities of both electrons (μ_n) and holes (μ_p) are taken to be constants and in most cases, Auger recombination which dominates at high-level injection (HLI) is neglected. In addition, quasi-neutrality ($\Delta n \approx \Delta p$) is assumed throughout the bulk, which allows the transport equations for both majority and minority carriers to be decoupled. These simplifications lead to analytical solutions which are only valid at low injection condition and consequently, only the asymptotic mono-exponential decay of excess carrier density is well-described [22], [25]. The multi-exponential decay of excess carrier density at early time-scale (HLI), which contains a wealth of information, is discarded as a result. By accurately modeling the dynamics at HLI,

the accuracy in decoupling can be improved, and parameters like the Auger coefficients for electrons (C_n) and holes (C_p) can also be obtained.

To model the high-injection condition accurately, it is important to consider the coupled transport equations of the majority and minority carriers and at the same time, and to take into account injection-dependent lifetime models, concentration-dependent mobilities, and the presence of a built-in electric field due to the difference in μ_n and μ_p. To this end, TCAD device simulator is used to solve the set of governing equations comprehensively. In the following sections, the governing transport equations and various models used in TCAD simulation will be described.

3.2 Optical Generation

3.2.1 Gaussian Light Pulse

As the experiment involves monochromatic illumination to generate excess carriers in a sample, knowledge of the spatial distribution of photo-generated carriers per unit time and volume within the absorber material is required. TCAD provides the flexibility of specifying the properties of the light signal that is incident on the sample and subsequently, solving for the carrier profiles upon illumination. These properties include the wavelength [nm], photon flux [N/cm^2], and the time profile

of the light pulse. In this work, the incident light pulse from the laser is modeled

using a Gaussian time function expressed as:

$$F(t) = \exp\left(-\left(\frac{t - t_1}{\sigma}\right)^2\right), \qquad t \geq t_1 \tag{3.1}$$

where t_1 is the time when the light pulse interacts with sample and σ is defined as

the FHWM of the light pulse.

3.2.2 Generation Rate

Given the properties of the illuminating light pulse, the optical generation rate,

$G(\lambda,z,t)$ [$cm^{-3}s^{-1}$], along the depth (z) of the sample can be computed using the

following equation:

$$G(\lambda, z, t) = J_0 F_{xy} F(t) \alpha(\lambda) exp\left(-\left|\int_{z'=0}^{z'=z} \alpha(\lambda) dz'\right|\right) \tag{3.2}$$

where J_0 [$cm^{-2}s^{-1}$] is incident photon intensity, F_{xy} is the shape factor where F_{xy}

equals 1 inside the defined illumination window and zero elsewhere, $F(t)$ is the

time function of the light pulse and $\alpha(\lambda)$ is the absorption coefficient of the sample

as a function of λ.

47

3.3 Carrier Transport

3.3.1 Continuity Equations

Outside thermal equilibrium, the rate of change of carrier concentrations in a control volume (CV) inside a semiconductor is determined by the imbalance of the generation and recombination rates in that CV as well as the flow of carriers in and out of the CV. The continuity equations for both electrons and holes capture this dynamics. The continuity equations are in essence a 'book-keeping' relationship that keep track of the carrier concentration in the CV and are expressed as:

$$\frac{\partial n}{\partial t} = G_{\text{net}} - R_{\text{net}} + \frac{1}{q}\vec{\nabla} \cdot \vec{J_e}$$

$$\frac{\partial p}{\partial t} = G_{\text{net}} - R_{\text{net}} - \frac{1}{q}\vec{\nabla} \cdot \vec{J_h}$$

(3.3)

where G_{net} is the net generation rate, R_{net} is the net recombination rate and $\vec{J_e}$ and $\vec{J_h}$ are the electron and hole current densities respectively.

3.3.2 Drift-diffusion Model

The drift-diffusion model is the simplest model to account for flow of carriers in and out of the CV under the influence of electric field (drift) and concentration gradient (diffusion). The current densities $\vec{J_e}$ and $\vec{J_h}$ are given by:

48

$$\vec{J_e} = -qn\vec{v}_e^{\mathrm{drift}}(E) + \frac{kT}{q}\mu_e\vec{\nabla}n$$

$$\vec{J_h} = qp\vec{v}_h^{\mathrm{drift}}(E) + \frac{kT}{q}\mu_h\vec{\nabla}p \tag{3.4}$$

where k is the Boltzmann constant, T is the temperature, $\vec{v}_e^{\mathrm{drift}}(E)$ and $\vec{v}_h^{\mathrm{drift}}(E)$ are the drift velocities of electrons and holes as a function of the electric field E.

The electric field is governed by the Gauss' law given by:

$$\vec{\nabla}\cdot\vec{E} = \frac{q}{\epsilon}(p - n + N_D^+ - N_A^-) \tag{3.5}$$

where ϵ is the electrical permittivity and N_D^+ and N_A^- are the fixed charge densities associated with the donor and acceptor atoms respectively.

In the limit of low E, $\vec{v}_e^{\mathrm{drift}}(E)$ and $\vec{v}_h^{\mathrm{drift}}(E)$ can be further expressed as a linear function of the μ and E:

$$\vec{v}_e^{\mathrm{drift}}(E) = \mu_e E$$

$$\vec{v}_h^{\mathrm{drift}}(E) = \mu_h E \tag{3.6}$$

Equations 3.3–3.6 provide the set of conditions necessary to study carrier dynamics in semiconductors. In the following sections, the models used to describe the degradation of carrier mobilities, the various recombination mechanisms and surface recombination will be discussed.

49

3.4 Doping-dependent Mobility Degradation

In doped semiconductors, the scattering of electrons and holes by fixed charged impurity dopant ions leads to degradation of μ_e and μ_h [26]. This phenomenon can be observed in Figure 3.1, which shows the electron and hole mobilities plotted against carrier concentration in phosphorous- and boron-doped silicon respectively.
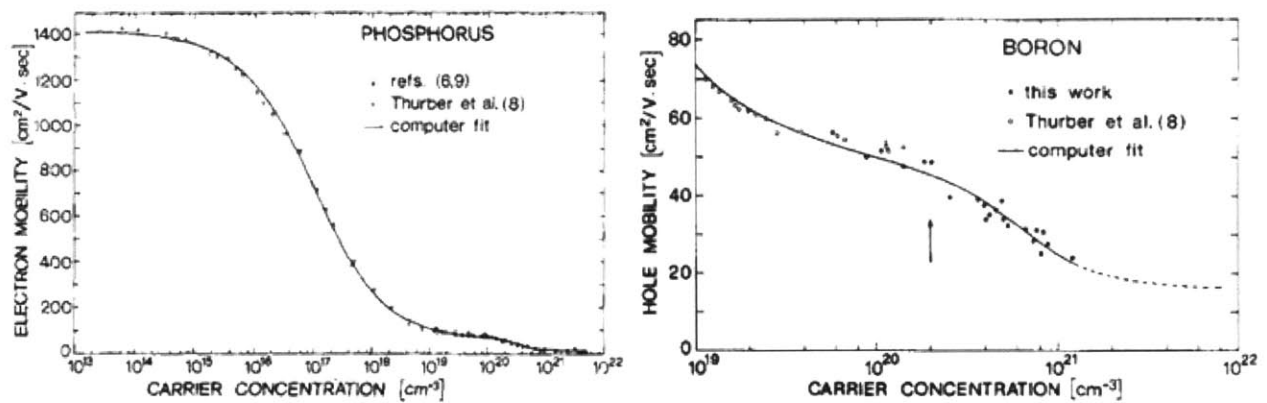
Figure 3.1: Electron and hole mobilities plotted against carrier concentration in phosphorous- and boron- doped silicon respectively, from Reference [26]. The solid lines represent the fit using the Masetti model.

In silicon, the commonly used model is the Masetti model given by:

$$\mu_{dop} = \mu_{min1}\exp\left(-\frac{P_c}{N_{A,0} + N_{D,0}}\right) + \frac{\mu_{const} - \mu_{min2}}{1 + ((N_{A,0} + N_{D,0})/C_r)^\alpha} - \frac{\mu_1}{1 + (C_s/(N_{A,0} + N_{D,0}))^\beta} \quad (3.7)$$

and the corresponding values for silicon are given in Table 3.1 [26].

Table 3.1: Default values of silicon for the Masetti model, from Reference [26].

Symbol	Electrons	Holes	Unit
μ_{min1}	52.2	44.9	cm^2/Vs
μ_{min2}	52.2	0	cm^2/Vs
μ_1	43.4	29.0	cm^2/Vs
P_c	0	9.23×10^{16}	cm^{-3}
C_r	9.68×10^{16}	2.23×10^{17}	cm^{-3}
C_s	3.43×10^{20}	6.10×10^{20}	cm^{-3}
α	0.680	0.719	1
β	2.0	2.0	1

3.5 Models for Recombination Mechanisms

3.5.1 Radiative Recombination

Radiative band-to-band recombination is an intrinsic process where an electron in the conduction band and a hole in the valence band is annihilated and the excess energy is emitted in the form of a photon with an energy approximately equal to the bandgap. The radiative recombination model expresses the recombination rate as:

$$R_{net}^{rad} = B(np - n_i^2) \qquad (3.8)$$

where the coefficient B is related to the probability of a radiative transition, which depends strongly on the band structure of the semiconductor and n_i is the intrinsic carrier concentration. For silicon, $B = 4.73 \times 10^{-15}$ cm^3/s [27].

3.5.2 Shockley-Read-Hall Recombination

Bulk defects such as impurities and dislocations can create energy states within the bandgap of a semiconductor. Recombination through these defect states can be modeled using the SRH model given by:

$$R_{net}^{SRH} = \frac{np - n_i^2}{\tau_{p0}(n + n_1) + \tau_{n0}(p + p_1)}$$

(3.9)

and,

$$n_1 = n_i \exp(\frac{E_t - E_i}{kT})$$

$$p_1 = n_i \exp(-\frac{E_t - E_i}{kT})$$

(3.10)

where $E_t - E_i$ is the difference between the defect level and the intrinsic Fermi level. τ_{p0} and τ_{n0} are the so-called capture time constants and are expressed by:

$$\tau_{p0} = \frac{1}{\sigma_p v_{th} N_t}$$

$$\tau_{n0} = \frac{1}{\sigma_n v_{th} N_t}$$

(3.11)

where σ_n and σ_p are the capture cross sections of electrons and holes, v_{th} is the thermal velocity of the charge carriers and N_t is the concentration of the defect. Equations 3.9 to 3.11 provide the injection-dependent recombination rate or lifetime for the SRH model. In this work, it is assumed that $E_t - E_i$ equals zero (deep defect) and τ_{n0} and τ_{p0} are used as fit parameters in the SRH model.

As the main purpose of this work is to model the decay of carrier concentrations at high level injection (HLI) condition, it is useful to obtain a high injection limit of the SRH lifetime τ_{SRH}. By assuming quasi-neutrality and the definition in equation 2.3, it can be shown that:

$$\tau_{SRH}^{HLI} = \tau_{n0} + \tau_{p0} \tag{3.12}$$

3.5.3 Band-to-band Auger Recombination

In band-to-band Auger recombination process, an electron in the conduction band recombines with a hole in the valence band and the excess energy and momentum is transferred to another electron or hole. The total Auger combination rate can be expressed as:

$$R_{net}^{Auger} = C_n n^2 p + C_p n p^2 \tag{3.13}$$

where C_n and C_p are the rate constants for the electron-electron-hole (eeh) and electron-hole-hole (ehh) processes respectively. The rate constants C_n and C_p are well characterized by many authors [28–30], in particular, the most cited values are

53

those determined by Dziewior *et al.* [28]. It is observed that both C_n and C_p are constants at high doping levels and injection-dependent at lower doping levels. Consequently, several Auger parameterization models have been proposed in order to describe this phenomenon [30], [31], including the widely-used parametric model developed by Kerr and Cuevas [30]. While the Kerr and Cuevas model can describe the injection dependence of Auger recombination, it cannot be used in numerical device modeling as it is a polynomial expression with a crude derivative [27]. Furthermore, the parametric model is derived based on the quasi-neutrality assumption ($\Delta n \approx \Delta p$) which might not necessary be a good approximation since an imbalance of charge due to $\mu_e \neq \mu_h$ can exist at HLI.

For the purpose of this work, the fundamental expression for the Auger recombination rate will be used and C_n and C_p will be treated as constants and fitting parameters.

3.5.4 Surface Recombination

To solve the PDE given in equation 3.3, appropriate boundary condition is required. In this work, the recombination of electron and holes at the boundaries is modeled using the surface SRH recombination model given by [32]:

$$R_{\text{net}}^{\text{surf,SRH}} = \frac{np - n_i^2}{\frac{1}{S_{p0}}(n + n_1) + \frac{1}{S_{n0}}(p + p_1)}$$

(3.14)

54

and,

$$n_1 = n_i \exp(\frac{E_t - E_i}{kT})$$

$$p_1 = n_i \exp(-\frac{E_t - E_i}{kT})$$

(3.15)

where S_{p0} and S_{n0} [cm/s] are the surface recombination velocities of electrons and holes respectively.

As the main purpose of this work is to model the decay of carrier concentrations at HLI, it is useful to obtain a HLI limit of the SRV, S_{eff}. It can be shown that for a p-type material:

$$S_{eff} = \frac{S_{n0}}{1 + \frac{S_{n0}}{S_{p0}}}$$

(3.16)

3.5.5 Simulation Models and Parameters

Having described the various models used in previous sections, Table 5.2 summarizes all the recombination parameters used in numerical simulation. A total of four fit parameters are used for SRH bulk and surface recombination. However, the number of fit parameters can be further reduced to two by assuming asymmetrical electron and hole lifetimes [27] and equal electron and hole surface recombination velocities.

Table 3.2: Summary of various recombination models and parameters used in the simulation.

Input Models	Input Parameters
Radiative recombination	$B=4.73\times10^{-15}$ cm^3/s
Auger recombination [a]	$C_n=2.8\times10^{-31}$ cm^6/s $C_p=7.91\times10^{-32}$ cm^6/s

Fit Models	Fit Parameters
SRH bulk recombination [b]	τ_{n0} and τ_{p0}; assume $\tau_{p0}=10\tau_{n0}$
SRH surface recombination [c]	S_{n0} and S_{p0}; assume $S_{n0}=S_{p0}$

[a] The Auger coefficients here are used as starting points and refined to improve the fit at HLI.
[b] Asymmetrical lifetimes is assumed; $\tau_{p0}=10\tau_{n0}$ [27].
[c] $S_{n0}=S_{p0}$ is assumed for simplicity.

3.6 TCAD Modeling: Sentaurus Package

3.6.1 Introduction to TCAD

Technology Computer-Aided Design (TCAD) refers to the use of computer simulations to model and optimize the fabrication process and performance of semiconductor devices. From the device perspective, the TCAD software solves the fundamental and governing equations using numerical methods to predict the electrical, optical and thermal behavior of semiconductor devices in response to external electrical, optical or thermal excitation. The Sentaurus TCAD by Synopsys is one such software [6]. The Sentaurus package is a collection of

56

simulation tools which have the ability to design the device structure, simulate the electrical, optical and thermal response and automate the optimization process. The tools which have been used in this thesis will be described in the next few sections.

3.6.2 Sentaurus Structure Editor

Sentaurus Structure Editor (SSE) is a tool used to design the 2D or 3D structure of a semiconductor device before simulation. It uses an input file written by the user to define the physical, structural and geometrical properties of the device. The SSE also has a meshing function in which the device is divided into discrete points spatial on which the governing equations will be solved. The output file contains the geometrical, physical, contact and chemical information about the device and is required by other tools down the line to perform simulations.

3.6.3 Sentaurus Device

Sentaurus Device (SD) is a tool used to solve the governing set of equation described in the earlier part of this chapter numerically at each mesh point, taking into account the models that are used to describe the various physical parameters. The SD tool has the capability of performing transient, DC and AC simulations and the output files contain information pertaining to the electrical, optical and thermal properties inside the device at the pre-defined time steps. This information

typically includes spatial distribution of carrier densities, electric field, potentials, quasi-Fermi levels and temperature etc.

3.6.4 Sentaurus Workbench

Sentaurus Workbench (SWB) is a tool designed to provide the framework for the integration of the other tools onto a single platform to make device simulation and optimization a more user-friendly process. It provides the capability to perform multiple simulations on a single device design by sweeping pre-defined parameters of interest. It calls each tool in the simulation line sequentially and passes on the output file to the next tool down the line upon successful completion. After each run, the user can choose to visualize the output characteristics of the device at any step along the simulation process.

4

SENSITIVITY OF DECOUPLING TECHNIQUE

4.1 Impact of Uncertainty on Sensitivity

As discussed in the previous chapter, most existing decoupling methods utilize the asymptotic mono-exponential part of the excess carrier density decay curve. As a consequence, the sensitivity of these techniques is limited to only certain regions in the S_{eff} and τ_b space where a unique solution can be obtained. In this chapter, it is of interest to determine the sensitivity of the newly proposed technique and at the same time, examine ways to enhance it.

In the fitting process, numerically generated data using TCAD is being fitted to the experimental data and the fit parameters S_{n0} and τ_{n0} can be obtained by minimizing the mean squared error (*MSE*) globally. In an ideal situation where there are no uncertainties of any kind, the *MSE* will be zero and a unique solution can be determined. However, the presence of uncertainties decreases the sensitivity of the technique and consequently, only upper and lower limits for the fit parameters that

exist within a reasonable error limit can be obtained. The two main limiting uncertainties that are identified here are experimental and parameter uncertainties. Experimental uncertainty is mainly due to electrical noise that is generated by the measurement equipment and is typically classified as random error. Such error can be reduced by repeating the measurements many times [33]. On the other hand, parameter uncertainty comes from the accuracy of the input parameters into the TCAD model, which cannot be controlled in the physical experiment and typically manifests itself as systematic error. It is of interest to gain an insight on the effect of these uncertainties on measurement sensitivity, and to determine a reasonable limit for *MSE* so that fit parameters that provide *MSE* lower than this pre-defined limit can be trusted to a certain level of confidence. In general, a large uncertainty leads to a large acceptable *MSE*. Hence more pairs of S_{n0} and τ_{n0} can satisfy the solution, resulting in lower sensitivity.

To this end, TCAD simulations are performed to help guide the analysis of error propagation and their effect on *MSE*, which is the figure-of-merit in the error minimization process. Figure 4.1 is a flow chart that summarizes the steps involved this goal. First, the uncertainties of the technique, both experimental and parameter, are characterized. Next, TCAD simulations are performed by sweeping through the region of interest (S_{n0}: 10^1 to 10^5 cm/s and τ_{n0}: 10^{-6} to 10^{-3} s) to calculate the correct decay signals at the two excitation wavelengths. Following

60

which, uncertainties will be artificially introduced into these signals to simulate actual experimental condition. Finally, the uncertainty-convoluted signals of each pair of S_{n0} and τ_{n0} are then fitted back to the exact solutions and the *MSE* values that are expected for a given noise distribution are calculated over the whole S_{n0} and τ_{n0} space.
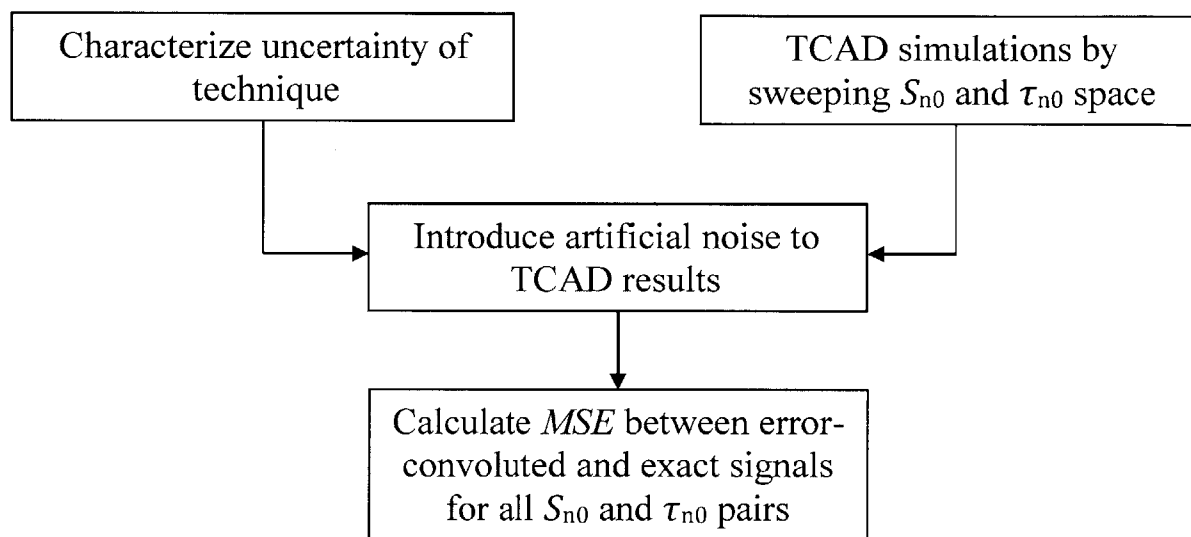
Figure 4.1: Flow chart illustrating the steps involved in determining a reasonable limit for *MSE*.

4.2 Characterizing Uncertainty

4.2.1 Random Error: Experimental Uncertainty

As first step, the random noise characteristics of the measurement tool are determined. Figure 4.2 shows the measured decay curve of excess carrier density in a 100 µm thin, p-type 1.3 $\Omega \cdot cm$, Al_2O_3 passivated, kerfless silicon wafer with a

61

1050 nm excitation light pulse and 1.55 μm probe beam. The signal trace is averaged over 1024 acquisitions in time steps of 0.5 ns.
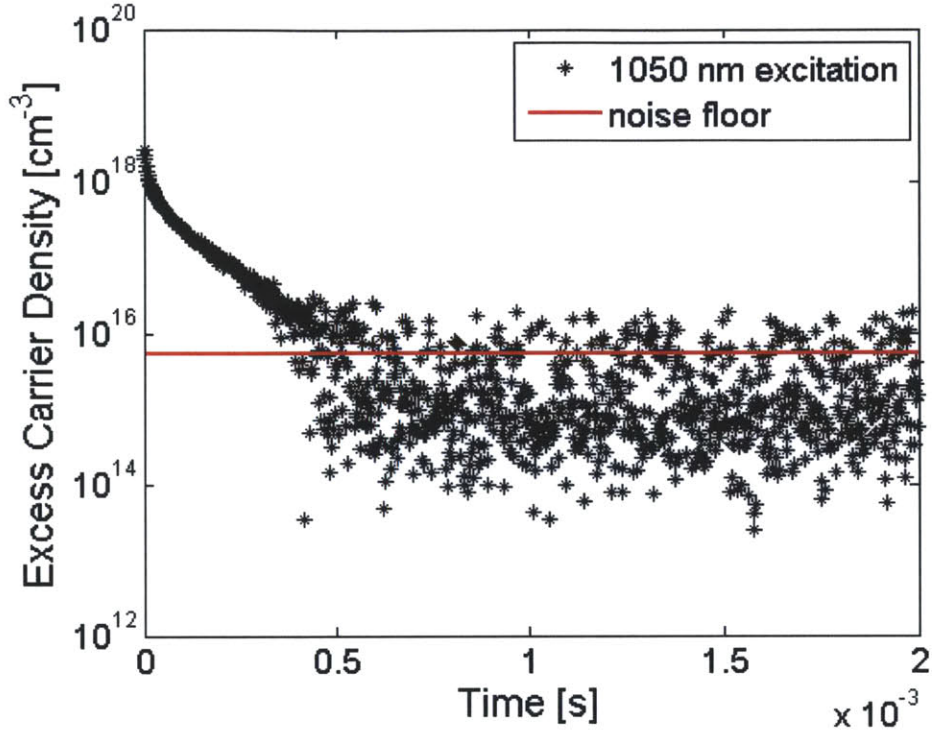
Figure 4.2: Transient decay of excess carrier density in control 100 μm thin kerfless c-Si sample measured using transient absorption pump-probe spectroscopy. The red line indicates the fit to the noise floor.

A clear decay signal can be observed at short time-scale. At longer time-scale ($t >$ 0.5 ms), a noise floor with random fluctuations can be observed. To determine the noise characteristics, the statistical distribution of the noise signal at long time scale is analyzed and represented using a histogram. As shown in Figure 4.3, the

noise is centered at $\mu = 5.5 \times 10^{15}$ cm^{-3} (noise floor) and has a standard deviation $\sigma = 4.3 \times 10^{15}$ cm^{-3}.
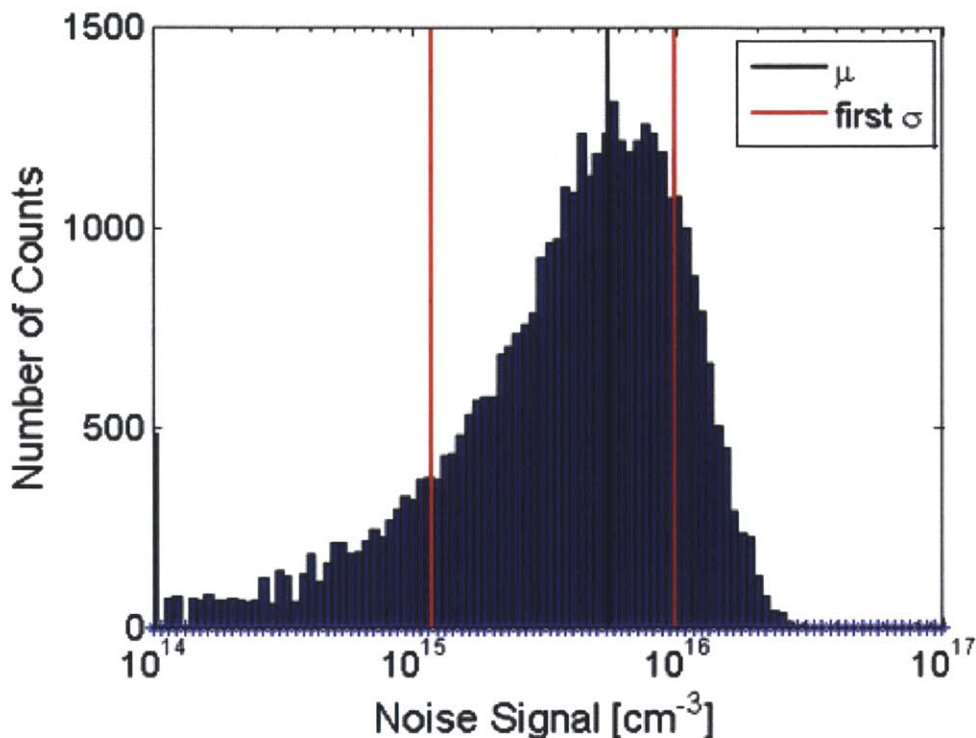
Figure 4.3: Histogram describing the statistical distribution of noise in the measurement tool.

The maximum resolvable excess carrier density is $\sim 1.0 \times 10^{16}$ cm^{-3} before the noise floor is reached. Comparatively, Linnros *et al.* [21] managed to obtain a lower noise floor at $\sim 1.0 \times 10^{14}$ cm^{-3} and this is most likely due to the difference in the wavelength used for the probe beam. They utilized a 3.39 μm probe laser beam that is far more sensitive to FCA, as observed in Figure 2.5. Looking forward, a possible improvement to enhance sensitivity will be to use a probe source with a longer infrared wavelength.

4.2.2 Systematic Error: Parametric Uncertainty

Random experimental error is not the only source of error in the experiment. Another possible source of error is the inaccuracy (over- or under-estimation) of input parameters used in the model or otherwise known as parameter uncertainty. The interest of this work focuses on modeling the HLI part of the decay curve and in this regime, Auger recombination contributes significantly towards recombination. The challenges in modeling or parameterizing the Auger coefficients for electrons and holes, C_n and C_p, are highlighted in section 3.5.3. Generally, an over- or under- estimation of C_n and C_p in the TCAD model manifests itself in the form of systematic error in the simulated results. It is of interest here to examine how uncertainties in C_n and C_p propagate into the eventual simulated results.

As starting point, the following expression for electrons can be used [29],

$$\tau_{\text{Auger}} = \frac{1}{C_n(\Delta n)^2} \tag{4.1}$$

The uncertainties of C_n and Δn are related by the following expression [33],

$$\frac{\delta C_n}{|C_n|} = 2\frac{\delta(\Delta n)}{|\Delta n|} \tag{4.2}$$

where $\frac{\delta C_n}{|C_n|}$ and $\frac{\delta \Delta n}{|\Delta n|}$ are the fractional uncertainties of C_n and Δn respectively and the uncertainty in time is neglected. Finally, the uncertainty of Δn can be expressed as,

$$\delta(\Delta n) = 0.05|\Delta n| \tag{4.3}$$

where $\frac{\delta C_n}{|C_n|}$ is assumed to be 20%. With this relationship, it can be observed that the parameter uncertainty is a function of Δn.

4.3 Mean Squared Error

The fit parameters are extracted by minimizing *MSE* between the actual experimental measurements and simulated results over the two excitation wavelengths and the *MSE* is expressed as [33]:

$$MSE = \sum_{\lambda=750,1050nm} \frac{\sqrt{\sum_N \left(\log_{10} A_{model}\,(S,\tau,\lambda) - \log_{10} A_{experimental}\right)^2}}{N} \tag{4.4}$$

where $A_{model}(S,\tau,\lambda)$ is the exact simulated signal predicted using TCAD simulations, $A_{experimental}$ is the experimental data and N is the number of data points. The logarithmic function is being used as the signal varies over > 2 orders of magnitude. For the noise fluctuations measured in section 4.3, it is of interest to determine a reasonable bound for *MSE*.

4.4 Modeling Effects of Uncertainties on *MSE*

The purpose of this section is to determine a reasonable limit for *MSE* such that fit parameters that have *MSE* lower than the pre-determined value can be trusted with high confidence during the fitting process. TCAD simulation is being used to achieve this objective. By modeling the uncertainties using probability density functions, the expected *MSE* values for all possible pair of S_{n0} and τ_{n0} combinations are calculated using the steps described in Section 2.5. In the following section, two different ways of modeling uncertainties are explored and discussed.

4.4.1 Random Error

In order to capture the random nature of the uncertainty, the noise is modeled using a normal distribution that is centered at zero with $\sigma = 4.3\times10^{15}$ cm^{-3}. The σ used in this case corresponds to the noise fluctuations measured in section 4.2.1. To replicate actual experimental condition, averaging (256 times) is being performed to statistically reduce random noise. In addition, to test the effect of a reduced noise fluctuation, one additional scenario with $\sigma = 2.0\times10^{15}$ cm^{-3} is also simulated. The results are summarized in Figure 4.4.

From Figure 4.4(a), it can be observed that for both cases, *MSE* has a spread of ±0.01 and varies as a function of S_{n0} and τ_{n0}. In the region of high S_{n0} and low τ_{n0},

MSE is low while vice versa in the region of low S_{n0} and high τ_{n0}. This phenomenon can be attributed to the properties of a logarithmic function. It can be shown that a small fluctuation, δy, in linear space can be expressed in terms of a small fluctuation, δz, in the logarithmic space through the relation:

$$\delta z \approx dz = d[\log(y)] = \frac{dy}{\ln(10)\,y} \approx 0.434\frac{\delta y}{y}$$

$$=> \delta z \approx 0.434\frac{\delta y}{y}$$

(4.5)

It is clear that for a fixed fluctuation δy in linear space, the resulting fluctuation δz is relatively smaller at HLI due to the factor $1/y$. Consequently, the *MSE* is weighted more towards lower injection, explaining the trend observed in Figure 4.4. By comparing all two cases, σ can result in an increase in sensitivity as the expected *MSE* are lower, with maximum *MSE* to be 0.050 for $\sigma = 4.3 \times 10^{15}$ cm^{-3} and 0.022 for $\sigma = 2.0 \times 10^{15}$ cm^{-3}. In general, σ can be reduced by using a more sensitive photodetector or a probe beam with a longer wavelength that is more sensitive to FCA as discussed earlier.

In conclusion, the sensitivity of the technique depends strongly on the effective lifetime of the sample for a random background noise. Reducing σ can lead to better instrumental sensitivity.
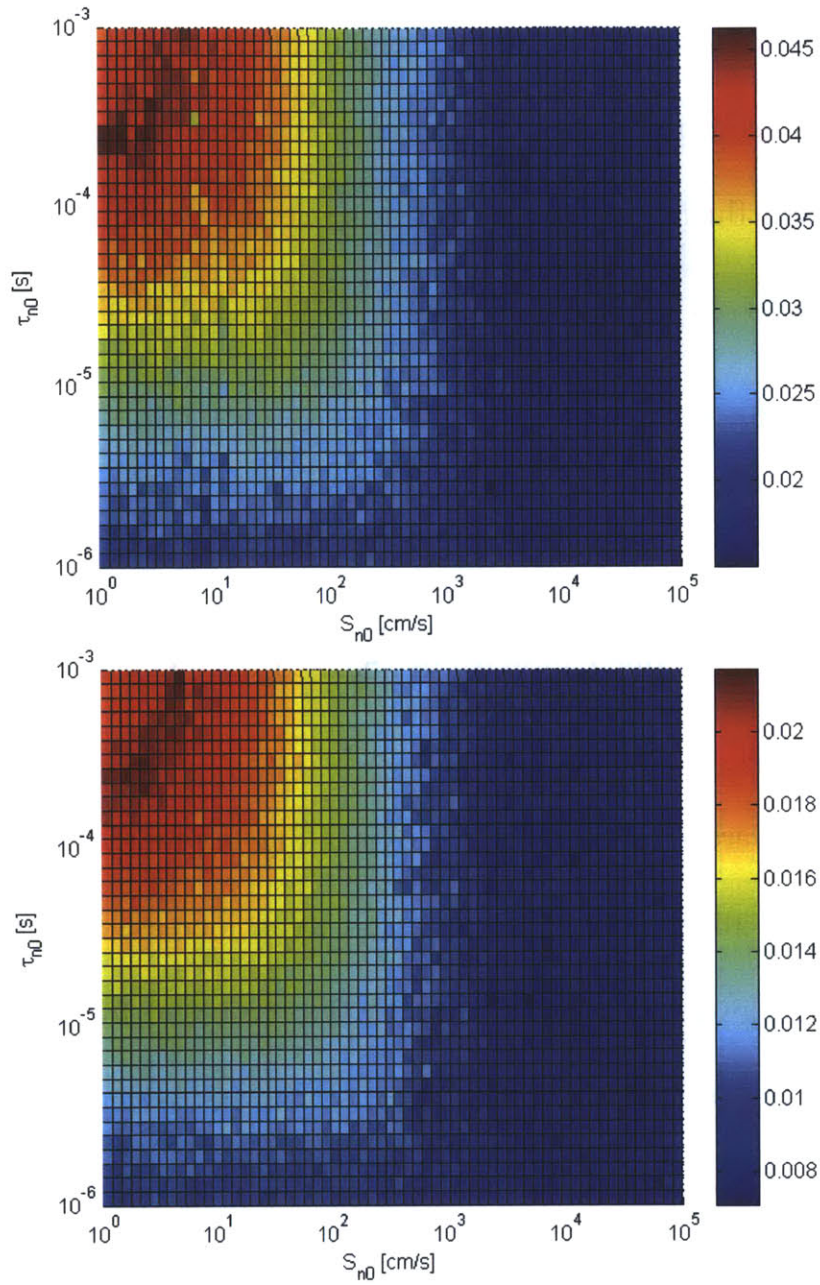
Figure 4.4: Top shows the *MSE* values for $\sigma = 4.3 \times 10^{15}$ cm^{-3} and bottom shows the corresponding *MSE* values for $\sigma = 2.0 \times 10^{15}$ cm^{-3}.

4.4.2 Random and Systematic Error

To model the combined effect of random and systematic errors, the instantaneous uncertainty is modeled using a normal distribution with an injection-dependent mean ($\mu = 0.05\Delta n$ cm^{-3}) and $\sigma = 4.3 \times 10^{15}$ cm^{-3}. The non-zero μ captures the systematic nature of the error as discussed in section 4.2.2. Figure 4.5 summarizes the calculated *MSE* values expected for the given noise distribution across the fitting parameter space. As compared to the values obtained solely by considering, the calculated MSE values have a lower spread (± 0.004). As a conservative estimate, a reasonable value for *MSE* that will be used in the fitting process in subsequent fitting analysis will be **0.060**.
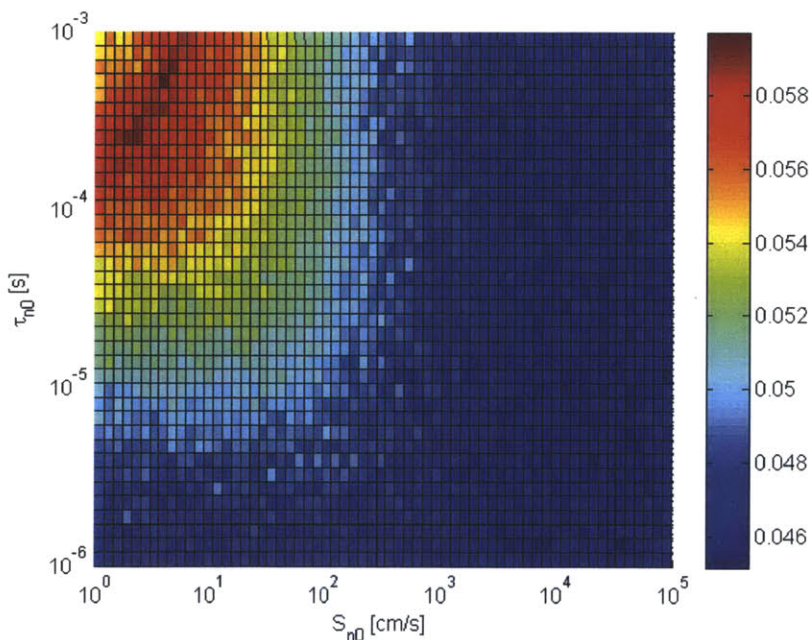
Figure 4.5: The calculated *MSE* values taking into account both random and systematic errors across the whole fitting parameter space. A fractional uncertainty of 10% is assumed for the Auger coefficients.

69

5

DECOUPLING BULK AND SURFACE-LIMITED LIFETIMES

5.1 Experimental Details

To understand the capabilities of the proposed technique, a total of four samples are characterized using the procedures described in Figure 2.8 and the results are compared to the Sinton PCD lifetime measurement tool. The sample conditions are summarized in Table 5.1. Two samples are 260 μm high-quality double-side polished float-zone (FZ) quality mono c-Si wafers. One of the FZ c-Si wafers is unpassivated and the other is passivated on both sides with a 10 nm layer of Al_2O_3 using atomic layer deposition (ALD), followed by a low-temperature 200°C anneal. Thin-film Al_2O_3 is a technique well-known to provide excellent surface passivation on a c-Si surface [12]. The remaining two samples are 100 μm thin kerfless mono c-Si wafers. Both kerfless wafers are subjected to phosphorous diffusion gettering (PDG) and one of the kerfless wafers is characterized without any surface treatments and the other is subjected to the same Al_2O_3 passivation

71

mentioned before. Prior to the ALD step, the wafers are subjected to a standard RCA clean to remove the surface native oxide. The main objective of this experiment is to determine the surface (S_{n0} and S_{p0}) and bulk SRH (τ_{n0} and τ_{p0}) recombination parameters of all samples. To reduce the number of constraints and for simplification, it is assumed here that $S_{n0} = S_{p0}$ and $\tau_{p0} = 10\tau_{n0}$ [27], leaving S_{n0} and τ_{n0} as the only fit parameters. The Auger coefficient (C_n and C_p) are refined manually to optimize the fit at injection condition $\Delta n > 5 \times 10^{17}$ cm^{-3}.

Table 5.1: Sample conditions used for lifetime characterization.

Sample	Growth Method	Thickness [um]	Resistivity [Ω/cm]	Pre-treatment	Bulk Treatment	Surface Passivation
1	FZ	260	2	-	-	-
2	FZ	260	2	RCA[a]	-	Al$_2$O$_3$[c]
3	Kerfless	100	1.3	-	PDG[b]	-
4	Kerfless	100	1.3	RCA[a]	PDG[b]	Al$_2$O$_3$[c]

[a] RCA clean.
[b] Phosphorus diffusion gettering.
[c] Double side passivation with 10 nm of Al$_2$O$_3$ by ALD followed by a low temperature 200°C anneal.

Decoupling the S_{n0} and τ_{n0} parameters in all four samples involves three main steps. Firstly, spectrally resolved transient absorption pump-probe spectroscopy is being used to measure the decay transients of the excess carrier density upon excitation by a laser pulse as described in Section 2.3.4. Next, the physical properties of the samples are used as inputs into TCAD simulations to predict the decay transients over the S_{n0} and τ_{n0} space. The sample structure used in the TCAD

model is illustrated schematically in Figure 5.1. Lastly, error minimization procedures developed in Chapter 4 are used separate the fit parameters S_{n0} and τ_{n0}. In addition, τ_{eff} of all samples are also measured using the Sinton lifetime tester tool and compared at the injection condition $\Delta n = 3 \times 10^{16}$ cm^{-3}. All results are summarized in Table 5.2 (page 82).
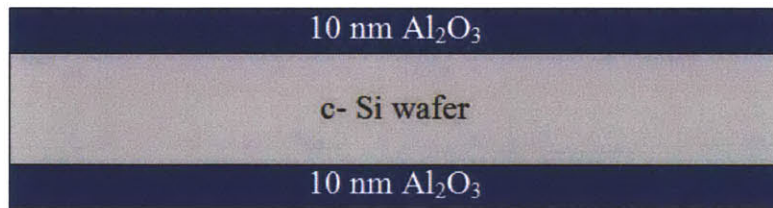
Figure 5.1: Sample structure used in TCAD simulations.

5.2 Results and Discussions

Figure 5.2 compares the measured and best-fit decay transient signals of all four samples using two different excitation wavelengths. The input and fit parameters in the simulation model for all four samples are summarized in Table 5.2 (page 82).

FZ c-Si   **Kerfless c-Si**
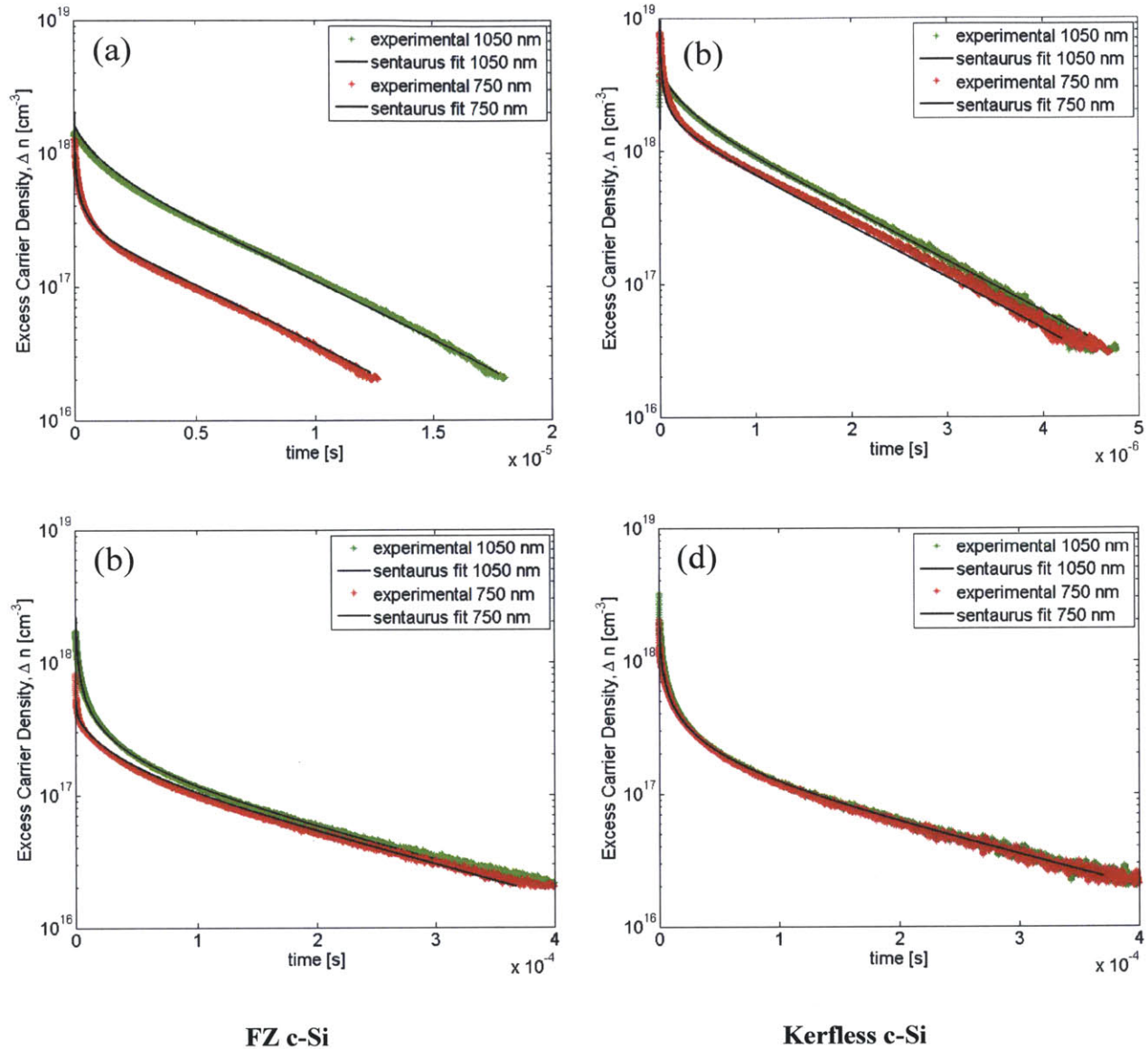
Figure 5.2: Measured (color symbols) and best fit (solid black line) decay transients of excess carrier density for (a) sample 1 (unpassivated), (b) sample 2 (passivated), (c) sample 3 (unpassivated) and, (d) sample 4 (passivated).

The MSE values for all pairs of S_{n0} and τ_{n0} are given in Figure 5.3 and Figure 5.4 for both sets of samples. The cut-off MSE used is 0.06, as represented by the black solid lines in the figures.

A typical decay curve can generally be divided into two regimes; the multi-exponential regime at short time-scale and the asymptotic mono-exponential decay at longer time-scale. At short time-scale, the wafer is in HLI and the non-linear effect of Auger recombination is dominant, leading to the observed multi-exponential decay. The multi-exponential effect is more pronounced with a shorter excitation wavelength. At 750 nm excitation, a higher density of excess carrier is generated nearer to the surface due to a shallower absorption depth, leading to more significant surface recombination during the initial phase of the decay [25].

For Sample 1, it can be observed from Figure 5.3 that S_{n0} is bounded in a narrow region centered at 1.6×10^4 cm/s with a well-defined global minimum and the value is consistent with that reported in literature for a c-Si surface with a layer of thin native oxide [34]. In comparison, the S_{n0} parameter for Sample 2 is bounded between 16 to 120 cm/s. The low S_{n0} value achieved by sample 2 can be attributed to the excellent surface passivating properties of the Al_2O_3 layer [12]. For sample 3, S_{n0} is bounded in a narrow region centered at 1.6×10^4 cm/s due to a well-defined global minimum and this value close to the value obtained for Sample 1, consistent for a native oxide/c-Si interface. For Sample 4, S_{n0} is bounded between 5 to 40 cm/s, reasonable range for Al_2O_3 passivated surface. In general, a reasonable lower and upper limit for S_{n0} can be determined for all samples.

For MSE = 0.06, an upper and lower limit for τ_{n0} can be obtained for both Samples 1 and 2 (FZ samples); 5 µs < τ_{n0} < 30 µs for sample 1 and 21 µs < τ_{n0} < 210 µs for Sample 2. As discussed in Section 3.5.2, a useful limit for τ_{SRH} at HLI (Δn = 3×10^{16} cm^{-3}) can be determine for both samples, where 0.05 ms < τ_{SRH}^{HLI} < 0.33 ms for Sample 1 and 0.23 ms < τ_{SRH}^{HLI} < 2.31 ms for Sample 2. However, only a lower bound can be obtained for τ_{n0} for both kerfless samples as observed in Figure 5.4; with τ_{n0} > 18 µs for Sample 3 and τ_{n0} > 21 µs for Sample 4. Similarly, the τ_{SRH} at HLI can be calculated; τ_{SRH}^{HLI} > 198 µs and τ_{SRH}^{HLI} > 231 µs for Samples 3 and 4 respectively. The high bulk lifetime measured for the kerfless c-Si wafers after gettering indicates good potential for these wafers to attain high-efficiency solar cells.

Lastly, the measured effective lifetimes at injection condition Δn = 3×10^{16} cm^{-3} here are also compared to the lifetimes measured by Sinton lifetime tester tool and reported in Table 5.2. The values measured by both techniques are close for all samples but a slight discrepancy exists for Sample 2 where the Sinton tool measured a slightly larger effective lifetime. However, the values are still comparable within the same order of magnitude and it should be noted that the discrepancy can be due to the fact that the FCA technique has a smaller active measurement area than the PCD technique.
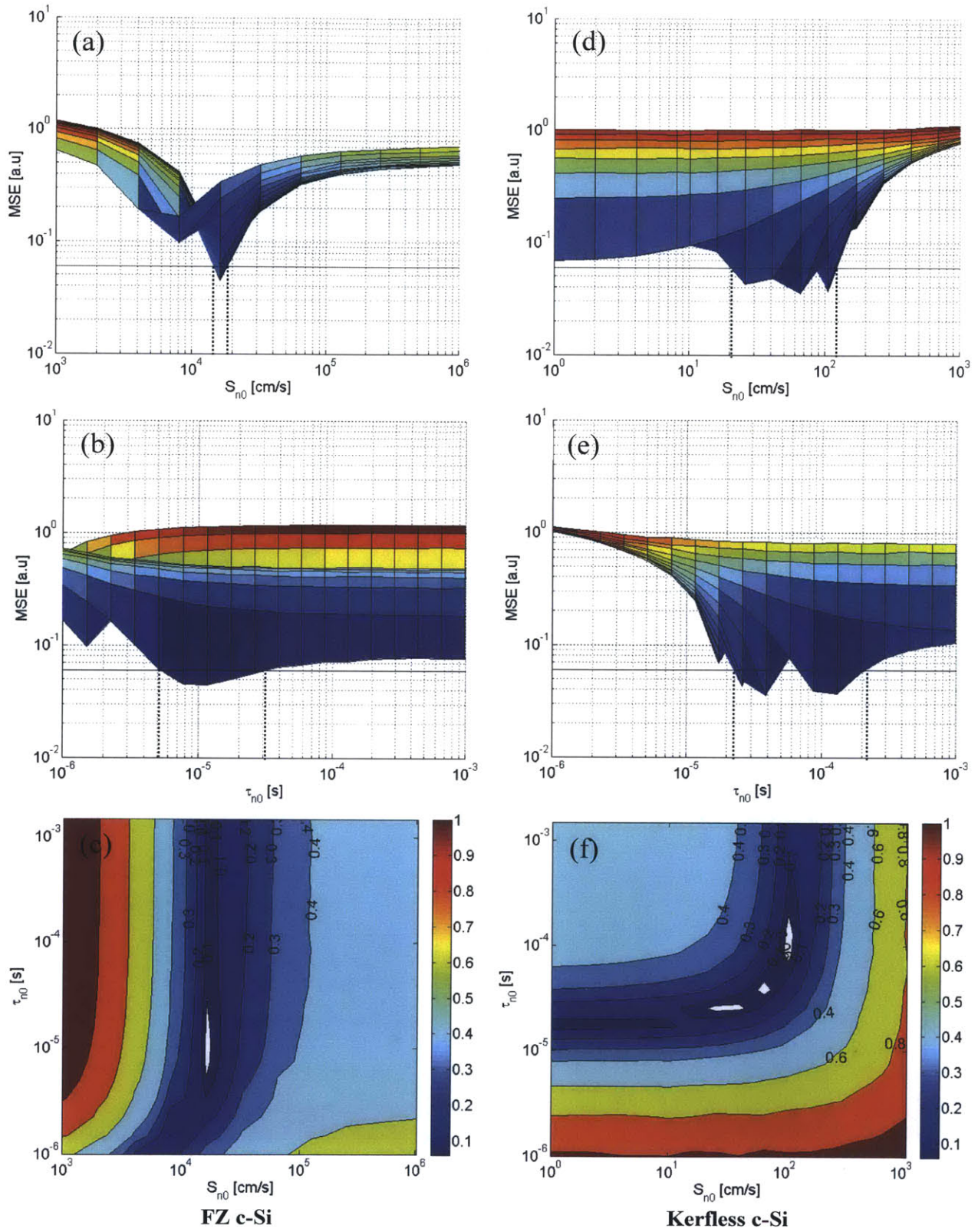
Figure 5.3: MSE values plotted against the fit parameters for Sample 1 (a to c) and Sample 2 (d to f)
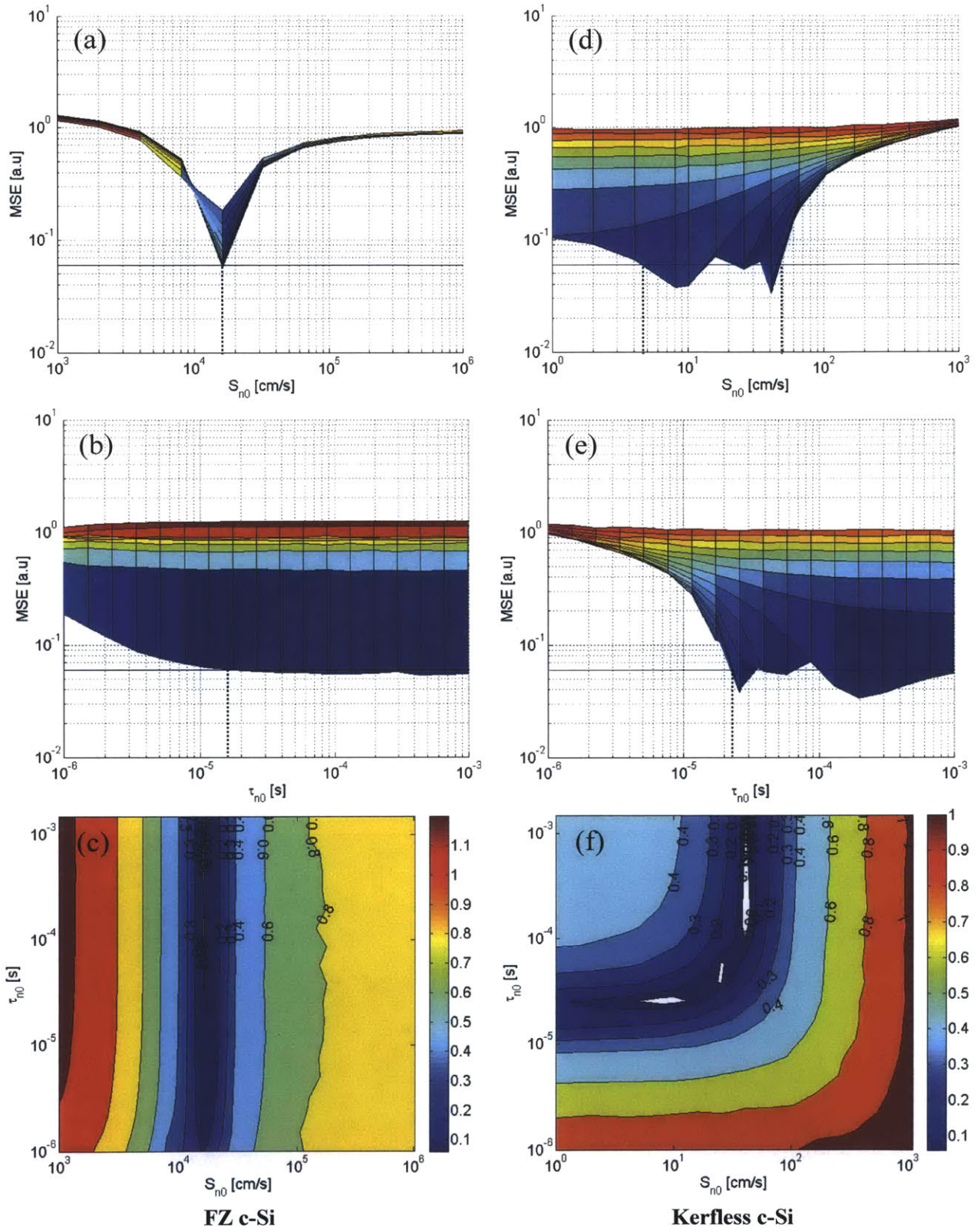
Figure 5.4: MSE values plotted against the fit parameters for Sample 3 (a to c) and Sample 4 (d to f)

5.2.1 Injection-dependent Lifetime

To gain insight on why only a lower limit for τ_{n0} can be achieved for the kerfless samples, the injection-dependent lifetimes for all samples are calculated and plotted in Figure 5.5. The injection-dependent contribution of the various recombination mechanisms are also estimated from the fit parameters (lower bound) using Equations 2.3–2.6 and included in the plots.

It can be observed that for all samples, the limiting mechanism at injection condition $\Delta n > 1 \times 10^{17}$ cm^{-3} is Auger recombination. Modeling the decay transients of excess carrier density in this regime can allow the Auger coefficients C_n and C_p be refined for all samples. At lower injection, both the SRH and surface recombination become significant. As denoted by Region A on Figure 5.5 (a) & (b), the SRH and surface lifetimes are comparable at the lower injection for the FZ samples, hence allowing the fit parameters be decoupled. In contrast, the effective lifetime in the thin kerfless samples quickly become either surface (Sample 3) or bulk (Sample 4) limited at lower injection condition due to the nature of a thin substrate, as shown in Figure 5.5 (c) & (d). Consequently, the sensitivity towards bulk-lifetime is reduced, allowing only a lower limit for τ_{n0} be determined. Nevertheless, it should be noted that by improving the sensitivity of the technique, especially by mitigating the effects of random error as discussed in Chapter 4, it should be possible to decouple both fit parameters for thinner wafers.

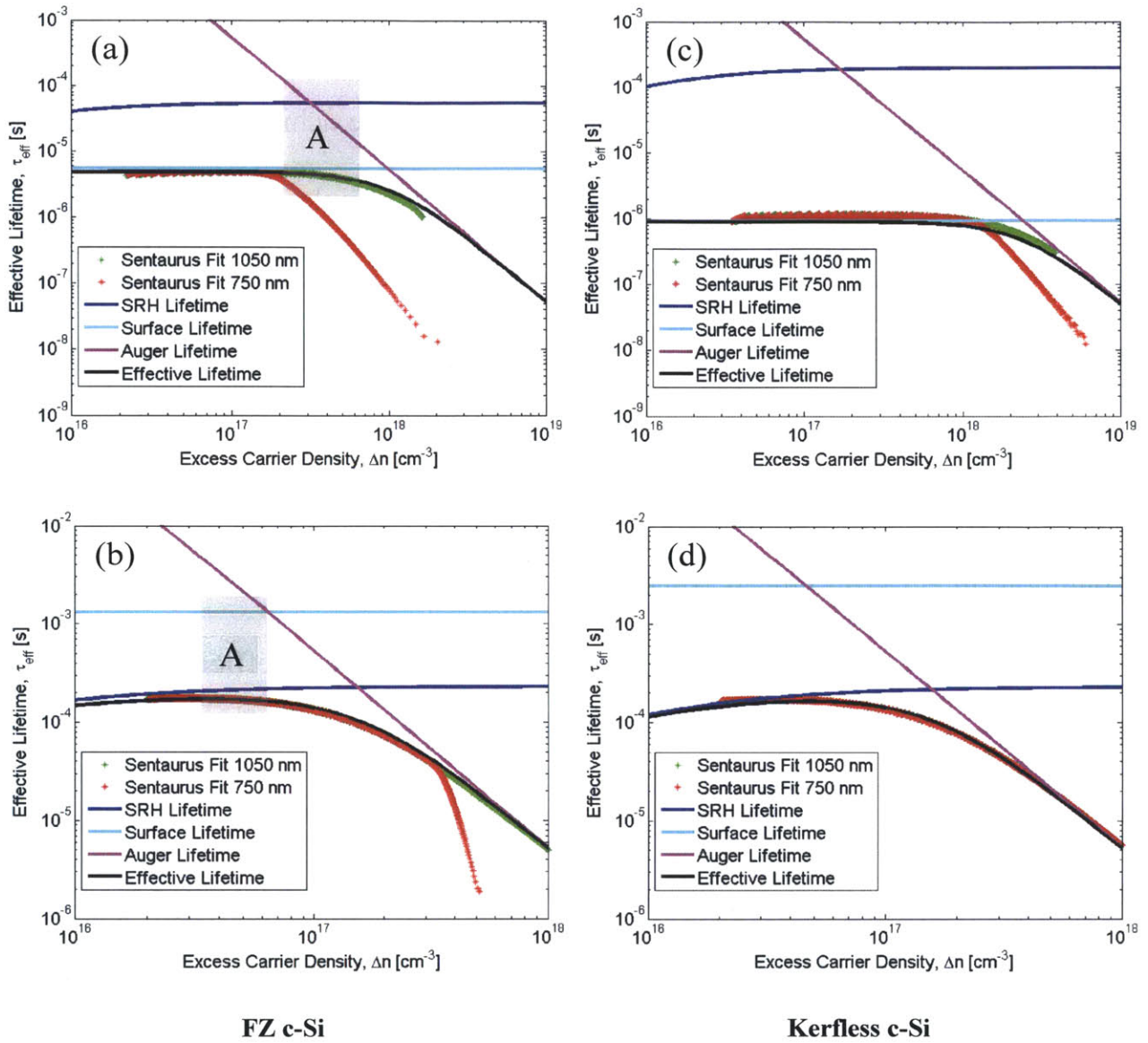**FZ c-Si**   **Kerfless c-Si**

Figure 5.5: Effective lifetime plotted against excess carrier density for (a) Sample 1, (b) Sample 2, (c) Sample 3 and, (d) Sample 4. The color symbols are obtained from the best-fit lines at the two excitation wavelengths and the color lines are the various recombination contributions to the effective lifetime estimated using the lower-bound fitted values.

80

5.3 Summary

It has been shown that by combining spectrally resolved pump-probe spectroscopy technique with TCAD simulations, reasonable bounds for the bulk and surface recombination parameters can be determined. The presence of random and systematic error limits the sensitivity and thus, the fit parameters cannot be determined uniquely. The measured effective lifetimes are further corroborated with PCD-based measurements using the Sinton lifetime tester tool.

For all four cases, reasonable upper and lower limits for S_{n0} can be obtained. The values obtained for each case are consistent with that reported for both Al_2O_3 and native SiO_2 surfaces. In addition, an upper and lower limit for τ_{n0} can be obtained for the FZ samples while only a lower limit for τ_{n0} can be determined for Samples 3 and 4. Injection-dependent effective lifetime calculations indicate that the lack of sensitivity occurs because the thin kerfless samples quickly become either surface- (Sample 3) or bulk- (Sample 4) limited at lower injection condition.

Finally, it is noted that it should be possible to decouple both fit parameters for thinner wafers by improving the sensitivity of the technique, especially by reducing random error.

Table 5.2: Summary of results, including the input parameters into TCAD model, fit parameters and comparison with Sinton lifetime tester tool.

Sample	Input Parameters		Fit Parameters				Effective Lifetimes	
	$C_n{}^a$ [cm^6/s]	$C_p{}^a$ [cm^6/s]	$\tau_{n0}{}^b$ [μs]	$\tau_{p0}{}^b$ [ms]	$S_{n0}{}^c$ [cm/s]	$S_{p0}{}^c$ [cm/s]	$\tau_{FCA}{}^d$ [μs]	$\tau_{PCD}{}^e$ [μs]
1	0.9×10^{-31}	7.6×10^{-32}	5-30	0.05-0.30	1.6×10^4	1.6×10^4	5	8
2	1.1×10^{-31}	7.8×10^{-32}	21-210	0.21-2.10	16-120	16-120	180	342
3	0.6×10^{-31}	7.3×10^{-32}	> 18	>0.18	1.6×10^4	1.6×10^4	1	3
4	0.9×10^{-31}	7.6×10^{-32}	> 21	>0.21	5-40	5-40	171	140

[a] The Auger coefficients are refined manually during the fitting process. The starting point is obtained from reference [28].
[b] Asymmetrical lifetimes is assumed; $\tau_{p0}= 10\tau_{n0}$ [27].
[c] For the fitting process, it is assumed that $S_{n0}= S_{p0}$ for simplicity.
[d] The values for τ_{FCA} are given at injection condition of 3×10^{16} cm^{-3} as predicted by TCAD simulations since the FCA measurement technique is noise-limited at 1×10^{16} cm^{-3} injection condition. For Samples 3 and 4, the values are lower bounds, given the noise floor of the FCA technique.
[e] τ_{PCD} values measured using the Sinton lifetime tester tool and are given at injection condition of 1×10^{16} cm^{-3}. For samples 1 and 3, transient mode is used and for samples 2 and 4, the QSSPC mode is used.

CHAPTER

6

CONCLUSIONS

It has been shown that by combining spectrally resolved pump-probe spectroscopy technique with TCAD simulations, reasonable upper and lower limits for the surface and bulk recombination parameters can be determined for 260 μm thick FZ wafers. For kerfless 100 μm thin c-Si wafers, S_{n0} can be bound to between an upper and lower limit, but only a lower limit can be determined for τ_{n0}. Investigating the injection-dependent lifetime indicates that the lack of sensitivity occurs because the thin kerfless samples quickly become either surface-(unpassivated) or bulk-(Al_2O_3 passivated) limited at lower injection conditions. Improving instrumental sensitivity, especially by reducing experimental error, can possibly allow decoupling of both fit parameters for thinner wafers. One method to enhance the sensitivity is to use a probe beam with a longer wavelength.

REFERENCES

[1]   U.S. Department of Energy, International Energy Outlook 2011, http://www.eia.gov/forecasts/ieo/index.cfm, Accessed Jan 20 2013.

[2]   German Advisory Council on Global Change, World in Transition-A Social Contract for Sustainability, http://www.wbgu.de/fileadmin/templates/dateien/veroeffentlichungen/hauptg utachten/jg2011/wbgu_jg2011_kurz_en.pdf, Accessed Jan 20 2013.

[3]   Greentechsolar, PV News Annual Data Collection Results: 2010 Cell, Module Production Explodes Past 20 GW, http://www.greentechmedia.com/articles/read/pv-news-annual-data-collection-results-cell-and-module-production-explode-p/, Accessed Jan 20 2013.

[4]   D. M. Powell, M. T. Winkler, H. J. Choi, C. B. Simmons, D. B. Needleman, and T. Buonassisi, Energ. Environ. Sci., 5, 5874 (2012).

[5]   J. Schmidt and A. G. Aberle, J. Appl. Phys., 81, 6186 (1997).

[6]   Sentaurus. Synopsys, Mountain View, California.

[7]   M. A. Green, Prog. Photovolt.: Res. Appl., 327, 327 (1999).

[8]   J. L. Cruz-Campa, M. Okandan, P. J. Resnick, P. Clews, T. Pluym, R. K. Grubbs, V. P. Gupta, D. Zubia, and G. N. Nielson, Sol. Energy Mater. Sol. Cells, 95, 551 (2011).

[9]   Y. Tsunomura, Y. Yoshimine, M. Taguchi, T. Baba, T. Kinoshita, H. Kanno, H. Sakata, E. Maruyama, and M. Tanaka, Sol. Energy Mater. Sol. Cells, 93, 670 (2009).

[10] S. Tohoda, D. Fujishima, A. Yano, A. Ogane, K. Matsuyama, Y. Nakamura, N. Tokuoka, H. Kanno, T. Kinoshita, H. Sakata, M. Taguchi, and E. Maruyama, J. Non-Cryst. Solids, 358, 2219 (2012).

[11] T. Lauinger, J. Schmidt, A. G. Aberle, and R. Hezel, Appl. Phys. Lett., **68**, 1232 (1996).

[12] B. Hoex, J. Schmidt, P. Pohl, M. C. M. van de Sanden, and W. M. M. Kessels, J. Appl. Phys., **104**, 044903 (2008).

[13] C. W. Teplin, K. Alberi, M. Shub, C. Beall, I. T. Martin, M. J. Romero, D. L. Young, R. C. Reedy, P. Stradins, and H. M. Branz, Appl. Phys. Lett., **96**, 201901 (2010).

[14] K. Alberi, H. M. Branz, H. Guthrey, M. J. Romero, I. T. Martin, C. W. Teplin, P. Stradins, and D. L. Young, Appl. Phys. Lett., **101**, 123510 (2012).

[15] T. Buonassisi, A. A. Istratov, M. A. Marcus, B. Lai, Z. Cai, S. M. Heald, and E. R. Weber, Nat. Mater., **4**, 676 (2005).

[16] K. Hartman, M. Bertoni, J. Serdy, and T. Buonassisi, Appl. Phys. Lett., **93**, 122108 (2008).

[17] R. A. Sinton and A. Cuevas, Appl. Phys. Lett., **69**, 2510 (1996).

[18] F. P. Giles Ph.D. thesis, Purdue University, 1996.

[19] K. Bothe, R. Krain, R. Falster, and R. Sinton, Prog. Photovolt.: Res. Appl., **18**, 204 (2010).

[20] K. Schroder and R. Noel, IEEE J. Solid-State Circuits, **13**, 180 (1978).

[21] J. Linnros, J. Appl. Phys., **84**, 275 (1998).

[22] K. L. Luke and L. Cheng, J. Appl. Phys., **61**, 2282 (1987).

[23] E. Yablonovitch, D. L. Allara, C. C. Chang, T. Gmitter, and T. B. Bright, Phys. Rev. Lett., **57**, 249 (1986).

[24] H. M'saad, J. Michel, J. J. Lappe, and L. C. Kimerling, J. of Electron. Mater., **23**, 487 (1994).

[25] A. Buczkowski, Z. J. Radzimski, G. A. Rozgonyi, and F. Shimura, J. Appl. Phys., **69**, 6495 (1991).

[26] G. Masetti and S. Solmi, IEEE Trans. Electron. Devices, **30**, 764 (1983).

[27] P. P. Altermatt, J. Comput. Electron., **10**, 314 (2011).

[28] J. Dziewior and W. Schmid, Appl. Phys. Lett., **31**, 346 (1977).

[29] P. P. Altermatt, J. Schmidt, G. Heiser, and A. G. Aberle, J. of Appl. Phys., **82**, 4938 (1997).

[30] M. J. Kerr and A. Cuevas, J. of Appl. Phys., **91**, 2473 (2002).

[31] A. Richter, F. Werner, A. Cuevas, J. Schmidt, and S. W. Glunz, Energ. Proc., **27**, 88 (2012).

[32] F. J. Ma, G. G. Samudra, M. Peters, A. G. Aberle, F. Werner, J. Schmidt, and B. Hoex, J. Appl. Phys., **112**, 054508 (2012).

[33] J. Taylor, *An Introduction to Error Analysis - The Study of Uncertainties in Physical Measurements*, 2nd ed. (University Science Books, California, 1997).

[34] H. Mackel and A. Cuevas, Proceedings of the 3rd World Conference on Photovoltaic Energy Conversion, Osaka, Japan, **1**, 71 (2003).